Journal of Thermal Stresses, 27: 705–740, 2004

ISSN: 0149-5739 print/1521-074X online
DOI: 10.1080/01495730490440145

Taylor & Francis
Taylor & Francis Group

TRANSIENT THERMOELASTIC DEFORMATIONS OF A THICK FUNCTIONALLY GRADED PLATE

L. F. Qian and R. C. Batra
Department of Engineering Science and Mechanics
Virginia Polytechnic Institute and State University
Blacksburg, VA

We study transient thermoelastic deformations of a thick functionally graded plate with edges held at a uniform temperature and either simply supported or clamped. Either the temperature or the heat flux is prescribed on the top surface of the plate with the bottom surface of the plate kept at either a uniform temperature or thermally insulated. Stresses and deformations induced due to the simultaneous application of the transient thermal and mechanical loads are also computed. The problem is solved by using a higher order shear and normal deformable plate theory and a meshless local Petrov–Galerkin method. Only nodal coordinates are needed, and neither nodal connectivity nor a background mesh is employed. The validity of the method and of the computer code is established by comparing computed results with the analytical solution of the three-dimensional thermoelasticity equations for a simply supported plate. Results are then computed for clamped plates. It is found that the centroidal deflection and the axial stress induced at the centroid of the top surface of the plate are significantly influenced by boundary conditions at the plate edges.

Keywords clamped edges, higher order shear and normal deformable plate theory (HOSNDPT), meshless local Petrov–Galerkin (MLPG) method, transient thermo-mechanical loads

Structural components such as turbines, aircraft engines, and space vehicles are often exposed to very high temperatures and thermal shocks which inevitably induce severe thermal stresses that can cause catastrophic failure of materials. One way to mitigate this effect is to use functionally graded materials (FGMs). Material properties vary continuously in an FGM thereby eliminating sharp jumps in stresses at the interfaces between two distinct materials as may occur in a laminated composite. Lavendel and Goetzel [1] proposed a graded cermet for jet engine blades to exploit

Received 11 August 2003; accepted 5 January 2004.

This work was partially supported by the Office of Naval Research grant N00014-98-1-0300 with Dr. Y. D. S. Rajapakse as the program manager. Dr. L. F. Qian was also supported by the China Scholarship Council.

Address correspondence to R. C. Batra, Department of Engineering Science and Mechanics, Virginia Polytechnic Institute and State University, Blacksburg, VA 24061, USA. E-mail: rbatra@vt.edu

the high ductility and toughness of metals and high thermal strength of ceramics. FGMs have also been used for structural optimization (such as bamboo, a highly optimized naturally occurring FGM [2]), increasing electrical conductivity without impairing the thermal insulation of ceramics [3], improving adhesion [4], and enhancing biocompatibility [5].

In a functionally graded (FG) plate, material properties are generally assumed to vary continuously in the thickness direction only. The response of an FG plate to mechanical and thermal loads may be computed analytically, numerically, or experimentally. We are not aware of experimental results on FG plates subjected to transient thermal and mechanical loads. The analysis techniques may employ either three-dimensional (3D) thermoelasticity equations or two-dimensional (2D) plate theories. One could use either the finite element method (FEM), or the finite difference method or a meshless method to find an approximate solution of a given boundary-value problem. For an FGM made of two or more constituents, one also employs a homogenization technique, such as the Mori–Tanaka method [6], Hill's self-consistent approach [7], the mean-field theory (e.g., see [8]), the three-phase model [9], or the rule of mixtures [10]. Vel and Batra [11] have shown that the responses of an FG plate computed with the Mori–Tanaka and the self-consistent homogenization techniques differ from each other. Analytical solutions of 3D thermoelasticity equations for simply supported FG plates subjected to either time-independent mechanical and/or thermal loads or transient thermal loads with mechanical inertia neglected have been given by Vel and Batra [11, 12]; they [13] have also given an analytical solution for the vibrations of a simply supported FG plate. However, no analytical solution is available for any other type of boundary conditions at the edges. Even for simply supported FG plates subjected to transient thermomechanical loads, no analytical solution has been reported in the literature. Batra [14] analyzed by the FEM plane strain deformations of a circular cylinder made of a Mooney–Rivlin material with the two material parameters depending on the radial coordinate. Thus, except for special edge conditions and/or special geometries, one needs to find an approximate solution numerically.

There is an enormous amount of literature on finding approximate thermomechanical response of FG plates under different mechanical and thermal loads; only a few representative papers are mentioned here. Ootao et al. [15] have analyzed 3D transient thermal stresses in an FG hollow cylinder, and Ootao and Tanigawa [16] in an FG sphere. They approximated the body as being made of several layers of slightly different homogeneous materials. Kim and Noda [17] used a similar approximation and used Green's function method to find the 3D transient temperature distribution in the plate. Tanigawa et al. [18] have examined the bending of an inhomogeneous plate with thermal loads applied on a part of its top surface; other works on thermoelastic deformations of FGM plates may be found in the literature [11, 13, 15–18].

Rogers et al. [19] have employed the method of asymptotic expansion to analyze 3D static deformations of inhomogeneous plates. However, boundary conditions on the edges of the plate in their theory are applied in an average sense like those in 2D plate theories. Reddy and Cheng [20] have also used the method of asymptotic expansion to study the 3D thermoelastic deformations of an FG plate. If

boundary-layer effects near clamped and free edges can be neglected then the method of asymptotic expansion can also be used to study plate problems for different edge conditions.

Plate theories used to analyze mechanical deformations of an FG plate include the first-order shear deformation theory (FSDT) [21], the third-order shear deformation theory (TSDT) [22], and the higher order shear and normal deformation plate theory (HOSNDPT) [23, 24]. In the HOSNDPT, normal and tangential tractions prescribed on the top and the bottom surfaces of the plate are exactly satisfied, and the transverse normal and shear stresses are computed from equation of the plate theory rather than from the balance of linear momentum. The order of the theory can be adjusted to predict accurate results for thick plates. Cheng and Batra [21] related deflections of a simply supported FG polygonal plate given by the FSDT and the TSDT to that of an equivalent homogeneous Kirchhoff plate. Loy et al. [25] have studied vibrations of FG cylindrical shells using Love's shell theory.

Whereas the FEM has often been used to find an approximate solution of an initial-boundary-value problem, the use of a meshless method is gaining popularity now. Two recent books [26, 27] summarize developments in meshless methods that include the element-free Galerkin [28], the hp-clouds [29], the reproducing kernel particle [30], the smoothed particle hydrodynamics [31, 32], the diffuse element [33], the partition of unity FE [34], the natural element [35], meshless Galerkin methods using radial basis functions [36], the meshless local Petrov–Galerkin (MLPG) [37], the finite difference, and the collocation methods. The major difference between the FEM and a meshless method is in the generation of basis functions used to approximate a function. We use the MLPG method mainly because it does not require any background mesh to evaluate different integrals appearing in the weak formulation of the problem. Also, with no nodal connectivity needed, the effort required to prepare the input file is much less than that for the FEM. Table 1 compares the MLPG with the FEM for the analysis of an elastodynamic problem.

Here we use the HOSNDPT to analyze the transient thermoelastic problem of an FG plate with edges either simply supported or clamped. Other edge conditions can also be easily considered. The transverse normal and shear stresses are computed from equations of the plate theory rather than by integrating the balance of linear momentum with respect to the thickness coordinate. The plate equations are solved numerically by using the MLPG method [37].

The paper is organized as follows. Section 2 summarizes equations governing the 3D transient thermoelastic deformations of an inhomogeneous plate, and a weak formulation of the problem; section 2 also describes briefly the HOSNDPT. Section 3 gives the weak formulation of the problem, and section 4 the MLPG formulation. Section 5 lists equations used to deduce effective properties of an FG plate from those of its two constituents and their volume fractions. Computed results for different thermal loads and the two edge conditions are presented in section 6, where they are also compared with the analytical solution of Vel and Batra [11, 12] for a simply supported FG plate. Results computed for transient thermal loads with and without the consideration of inertia effects reveal that inertia forces have a negligible effect on the computed fields. However, when time-dependent thermal and mechanical loads are applied simultaneously then inertia forces significantly

Table 1 Comparison of the MLPG method and the FEM for an elastodynamic problem

	MLPG	FEM
Weak form	Local	Global
Information needed about nodes	Locations only	Locations and connectivity
Subdomains	Circular/rectangular, not necessarily disjoint	Polygonal and disjoint
Basis functions	Complex and difficult to express in closed form	Simple polynomials
Integration rule	Higher order	Lower order
Satisfaction of essential boundary conditions	Requires extra effort	Easy to enforce
Mass/stiffness matrices	Asymmetric, large band width that can not be determined apriori, not necessarily positive semidefinite	Symmetric, banded, mass matrix positive definite, stiffness matrix positive definite after imposition of essential boundary conditions
Sum of elements of mass matrix	Not necessarily equal to the total mass of the body	Equals total mass of the body
Assembly of equations	Not required	Required
Stresses/strains	Smooth everywhere	Good at integration points
Locking phenomenon for constrained problems	No	Yes
Addition of nodes	Easy	Difficult
Determination of time step size for stability in an explicit algorithm	Difficult, requires determination of the maximum frequency of the structure	Relatively easy
Computation of the total strain energy of the body	Difficult	Relatively easy
Imposition of continuity conditions at interfaces between two materials	Requires either consideration in the generation of basis functions or the use of Lagrange multipliers	Easy to implement
Data preparation effort	Little	Extensive

influence stresses and temperatures induced in the plate. Conclusions are summarized in the final section.

PROBLEM FORMULATION

Governing Equations

A schematic sketch of the problem studied and the rectangular Cartesian coordinate axes x_1, x_2, x_3 used to describe deformations of the FG plate are shown in Figure 1. It is assumed that the plate occupies the region $\Omega = [0, a] \times [0, b] \times [-h/2, h/2]$ in the unstressed reference configuration. The midsurface of the plate is denoted by $S = [0, a] \times [0, b] \times \{0\}$, and the boundary of S by Γ. The plate is made of isotropic

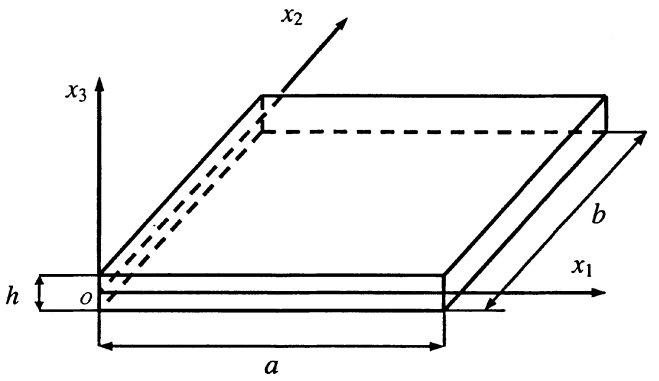

Figure 1. Schematic sketch of the problem studied.

materials with the macroscopic response also isotropic and material properties varying only in the thickness (x_3) direction.

In the absence of body forces and sources of internal energy, transient thermoelastic deformations of an isotropic plate are governed by

$$\sigma_{ij,j} = \rho\ddot{u}_i, \quad -q_{i,i} = \rho c\dot{T} \qquad \text{in } \Omega,\ t > 0,\ i,\ j = 1,2,3 \tag{1}$$

$$\sigma_{ij} = \lambda\varepsilon_{kk}\delta_{ij} + 2\mu\varepsilon_{ij} - \beta\delta_{ij}T \qquad q_j = -\kappa T_{,j}, \qquad \text{in } \Omega,\ t > 0 \tag{2}$$

$$\varepsilon_{ij} = (u_{i,j} + u_{j,i})/2 \qquad \text{in } \Omega,\ t > 0 \tag{3}$$

where $\boldsymbol{\sigma}$ is the stress tensor; ρ the mass density; $\boldsymbol{q}$ the heat flux; c the specific heat; $\boldsymbol{\varepsilon}$ the infinitesimal strain tensor; $\boldsymbol{u}$ the displacement; T the change in temperature from that in the stress-free reference configuration; a comma followed by j indicates partial differentiation with respect to x_j; a superposed dot indicates partial differentiation with respect to time t; a repeated index implies summation over the range of the index; $\boldsymbol{x}$ gives the position of a material particle; $\boldsymbol{\delta}$ is the Kronecker delta; λ and μ are Lamé constants; $\beta = 3K\alpha$ is the stress–temperature coefficient; K is the bulk modulus; α is the coefficient of thermal expansion; and κ is the thermal conductivity. Material parameters $\lambda,\ \mu,\ \beta,\ \rho,\ c,$ and κ are smooth functions of x_3. Equation $(1)_1$ expresses the balance of linear momentum, and Eq. $(1)_2$ the balance of internal energy. Equation $(2)_1$ is Hooke's law and Eq. $(2)_2$ the Fourier law of heat conduction. Henceforth, coordinates $x_1,\ x_2,$ and x_3 of a point are denoted by $x,\ y,$ and z, respectively.

Pertinent boundary and initial conditions considered are

$$\begin{aligned}
&\boldsymbol{\sigma}\mathbf{n} = \mathbf{f}(\mathbf{x}) \quad \text{on} \quad \Gamma_f \times \left[-\frac{h}{2}, \frac{h}{2}\right] \times (0,t) \\
&\mathbf{u} = \bar{\mathbf{u}} \qquad \text{on} \quad \Gamma_u \times \left[-\frac{h}{2}, \frac{h}{2}\right] \times (0,t) \\
&\boldsymbol{\sigma}\mathbf{n} = \mathbf{p}^{\pm} \quad \text{on} \quad S^{\pm} \times (0,t) \\
&\mathbf{q}\cdot\mathbf{n} = h^{\pm} \quad \text{on} \quad S^{\pm} \times (0,t)
\end{aligned} \tag{4}$$

$$T = \bar{T} \qquad \text{on} \quad \Gamma_T \times \left[-\frac{h}{2}, \frac{h}{2}\right] \times (0, t)$$
$$\mathbf{q} \cdot \mathbf{n} = \hat{q} \qquad \text{on} \quad \Gamma_q \times \left[-\frac{h}{2}, \frac{h}{2}\right] \times (0, t)$$

$$\begin{aligned} \mathbf{u}(x, y, z, 0) &= \mathbf{u}_0(x, y, z) \qquad \text{in } \Omega \\ \dot{\mathbf{u}}(x, y, z, 0) &= \dot{\mathbf{u}}_0(x, y, z) \qquad \text{in } \Omega \\ T(x, y, z, 0) &= T_0(x, y, z) \qquad \text{in } \Omega \end{aligned} \tag{5}$$

where Γ_u and Γ_f are parts of the lateral boundary of the plate where displacements and surface tractions are prescribed respectively; heat flux and temperature are prescribed, respectively, on Γ_q and Γ_T. On the top, S^+, and the bottom, S^-, surfaces of the plate, surface tractions are prescribed as $\mathbf{p}^+$ and $\mathbf{p}^-$, respectively, and the heat flux as h^+ and h^-, respectively. The initial displacement, velocity, and temperature are prescribed as $\mathbf{u}_0(x, y, z)$, $\dot{\mathbf{u}}_0(x, y, z)$, and $T_0(x, y, z)$, respectively. Instead of boundary condition $(4)_4$, one could also have

$$T(x, y, z, t) = T^{\pm}(x, y, z, t) \text{ on } S^{\pm} \times (0, t) \tag{6}$$

Substitution from Eqs. (2) and (3) into Eq. (1) yields field equations for the displacement $\mathbf{u}$ and the temperature T. These equations are one-way coupled in the sense that the field equation for T does not involve $\mathbf{u}$ but that for $\mathbf{u}$ involves T. Thus, the temperature field can be found first, and then displacements can be computed.

Brief Review of the Compatible HOSNDPT

We give details of the compatible HOSNDPT for the case of surface tractions and the heat flux prescribed on the top and the bottom surfaces. When temperature is assigned on these two surfaces, then the expansion for the temperature field should be modified as given by Qian and Batra [38].

By using Legendre polynomials in z orthonormalized by

$$\int_{-h/2}^{h/2} L_i(z) L_j(z)\, dz = \delta_{ij} \tag{7}$$

we write

$$\begin{aligned} \mathbf{u}(x, y, z, t) &= \left\{ \begin{array}{c} u(x, y, z, t) \\ v(x, y, z, t) \\ w(x, y, z, t) \end{array} \right\} = \sum_{i=0}^{K} \left\{ \begin{array}{c} u_i(x, y, t) \\ v_i(x, y, t) \\ w_i(x, y, t) \end{array} \right\} L_i(z) \\ T(x, y, z, t) &= \sum_{i=0}^{K} T_i(x, y, t) L_i(z) \end{aligned} \tag{8}$$

In Eq. (7), δ_{ij} is the Kronecker delta. Expansions (8) for the unknown fields have been used by Mindlin and Medick [39], who attributed them to W. Prager, Batra and Vidoli [24], and Batra et al. [40]. When $K \geq 3$, the plate theory is called higher order. Equation (8) elucidates that both transverse normal and transverse shear deformations are being considered. Expressions for $L_0(z), L_1(z), \ldots, L_5(z)$ are given in the Appendix. Since $L_i(z)$ is a polynomial of degree i in z, $L_i'(z) = dL_i/dz$ can be written as

$$L_i'(z) = \sum_{j=0}^{K} d_{ij} L_j(z) \tag{9}$$

where d_{ij} are constants.

For infinitesimal deformations, strains $\boldsymbol{\varepsilon}$ and temperature gradient $\mathbf{g}$ are given by

$$\boldsymbol{\varepsilon} = \begin{Bmatrix} \varepsilon_{xx} \\ \varepsilon_{yy} \\ \varepsilon_{zz} \\ 2\varepsilon_{yz} \\ 2\varepsilon_{zx} \\ 2\varepsilon_{xy} \end{Bmatrix} = \sum_{i=0}^{K} \begin{Bmatrix} \frac{\partial u_i(x,y)}{\partial x} \\ \frac{\partial v_i(x,y)}{\partial y} \\ \sum_{j=0}^{K} w_j(x,y)\, d_{ji} \\ \frac{\partial w_i(x,y)}{\partial y} + \sum_{j=0}^{K} v_j(x,y)\, d_{ji} \\ \frac{\partial w_i(x,y)}{\partial x} + \sum_{j=0}^{K} u_j(x,y)\, d_{ji} \\ \frac{\partial v_i(x,y)}{\partial x} + \frac{\partial u_i(x,y)}{\partial y} \end{Bmatrix} L_i(z) \equiv \sum_{i=0}^{K} \{\eta_i\} L_i(z) \tag{10}$$

$$\mathbf{g} = \begin{Bmatrix} \partial T/\partial x \\ \partial T/\partial y \\ \partial T/\partial z \end{Bmatrix} = \sum_{i=0}^{K} \begin{Bmatrix} \frac{\partial T_i}{\partial x} \\ \frac{\partial T_i}{\partial y} \\ \sum_{j=0}^{K} d_{ji} T_j \end{Bmatrix} L_i(z) = \sum_{i=0}^{K} \{\xi_i\} L_i(z)$$

where for $i = 0, 1, 2, \ldots, K$, η_i and ξ_i are six-dimensional and 3D vectors, respectively, with components given by

$$\begin{aligned}
&\eta_{i(1)} = \frac{\partial u_i}{\partial x} \qquad \eta_{i(2)} = \partial v_i/\partial y \qquad \eta_{i(3)} = \sum_{j=0}^{K} d_{ji} w_j \\
&\eta_{i(4)} = \frac{\partial w_i}{\partial y} + \sum_{j=0}^{K} v_j d_{ji} \qquad \eta_{i(5)} = \partial w_i/\partial x + \sum_{j=0}^{K} u_j\, d_{ji} \\
&\eta_{i(6)} = \frac{\partial v_i}{\partial x} + \frac{\partial u_i}{\partial y} \\
&\xi_{i(1)} = \frac{\partial T_i}{\partial x} \qquad \xi_{i(2)} = \frac{\partial T_i}{\partial y} \qquad \xi_{i(3)} = \sum_{j=0}^{K} d_{ji} T_j
\end{aligned} \tag{11}$$

Since $d_{ij} \not\equiv 0$, the transverse normal and the transverse shear strains for $K > 1$ depend on displacements $u_0, v_0, w_0, u_1, v_1, w_1, \ldots, u_{K-1}, v_{K-1}, w_{K-1}$, and the transverse temperature gradient depends on $T_0, T_1, \ldots, T_{K-1}$. Using constitutive relations (2), stresses and the heat flux at a point $\mathbf{x} = (x, y, z)$ are given by

$$\begin{aligned} \boldsymbol{\sigma} &= \{\sigma_{xx}\ \sigma_{yy}\ \sigma_{zz}\ \sigma_{yz}\ \sigma_{zx}\ \sigma_{xy}\}^T = \mathbf{D}^u \boldsymbol{\varepsilon} - \mathbf{D}^t T \\ \mathbf{q} &= \{q_x,\ q_y,\ q_z\}^T = \boldsymbol{\kappa} \mathbf{g} \end{aligned} \tag{12}$$

where $\mathbf{D}^u$ is the matrix of elastic constants, $\mathbf{D}^t$ the matrix of stress-temperature moduli, and $\boldsymbol{\kappa}$ the matrix of thermal conductivity. The plate has been assumed to be initially stress free. Substitution from Eqs. (10) and (11) into Eq. (12) gives stresses and the heat flux at the point (x, y, z) in terms of displacements, in-plane gradients of displacements, the temperature, and the in-plane gradients of temperature at the point (x, y) on the midsurface S.

We omit here derivation of the plate equations, which are given by Batra and Vidoli [24] for a piezoelectric plate based on the mixed variational principle of Yang and Batra [41], and by Batra et al. [40] for an elastic plate based on the Hellinger–Reissner principle.

It follows from Eq. (8) that

$$\dot{\mathbf{u}}(x, y, z, t) = \left\{ \begin{array}{c} \dot{u}(x, y, z, t) \\ \dot{v}(x, y, z, t) \\ \dot{w}(x, y, z, t) \end{array} \right\} = \sum_{i=0}^{K} \left\{ \begin{array}{c} \dot{u}_i(x, y, t) \\ \dot{v}_i(x, y, t) \\ \dot{w}_i(x, y, t) \end{array} \right\} L_i(z) \tag{13}$$

and a similar expression holds for $\ddot{\mathbf{u}}$. Knowing $\dot{\mathbf{u}}(x, y, z, 0)$, $\dot{u}_i(x, y, 0)$, $\dot{v}_i(x, y, 0)$, and $\dot{w}_i(x, y, 0)$ can be computed from Eq. (13) by multiplying both sides with $L_j(z)$and integrating the resulting expression with respect to z from $-h/2$ to $h/2$. One can similarly compute $u_i(x, y, 0)$, $v_i(x, y, 0)$, $w_i(x, y, 0)$, and $T_i(x, y, 0)$ from $\mathbf{u}(x, y, z, 0)$ and $T(x, y, z, 0)$.

WEAK FORMULATION OF THE PROBLEM

Let $\tilde{u}$, $\tilde{v}$, $\tilde{w}$, and $\tilde{T}$ be linearly independent functions defined on Ω. Like u, v, w, and T in Eq. (2), $\tilde{u}$, $\tilde{v}$, $\tilde{w}$, and $\tilde{T}$ are expanded in terms of Legendre polynomials in z. Multiplying the three equations $(1)_1$ expressing the balance of linear momentum in x, y, and z directions by $\tilde{u}$, $\tilde{v}$, and $\tilde{w}$, respectively, adding the three resulting equations, and using the divergence theorem, we obtain

$$\int_\Omega \tilde{\boldsymbol{\varepsilon}}^T \boldsymbol{\sigma}\, d\Omega - \int_{\partial\Omega} \tilde{\mathbf{u}}^T \boldsymbol{\sigma} \mathbf{n}\, dS + \int_\Omega \rho \tilde{\mathbf{u}}^T \ddot{\mathbf{u}}\, d\Omega = 0 \tag{14}$$

Similarly, Eq. $(1)_2$ gives

$$\int_\Omega \rho c \dot{T} \tilde{T}\, d\Omega + \int_\Omega \tilde{\mathbf{g}}^T \mathbf{q}\, d\Omega - \int_{\partial\Omega} \tilde{T} \mathbf{q} \cdot \mathbf{n}\, dS = 0 \tag{15}$$

where $\tilde{\boldsymbol{\varepsilon}}$ is the six-dimensional strain vector derived from the displacement $\tilde{\mathbf{u}} = (\tilde{u}, \tilde{v}, \tilde{w})$, $\tilde{\mathbf{g}}$ is the gradient of the temperature field $\tilde{T}$, and $\partial\Omega$ is the boundary of Ω. Substitution from Eqs. (10), (12), (4), and (5) into Eqs. (14) and (15), and integration with respect to z from $-h/2$ to $h/2$, give

$$\sum_{i,j=0}^{K}\left[\int_S \{\tilde{u}_i\}^T[m_{ij}]\{\ddot{u}_j\}\,dS + \int_S \{\tilde{\eta}_i\}^T[E^u_{ij}]\{\eta_j\}\,dS - \int_{\Gamma_u} \{\tilde{u}_i\}^T[N][E^u_{ij}]\{\eta_j\}\,d\Gamma\right]$$
$$= \sum_{i=0}^{K}\left[\int_{\Gamma_f} \{\tilde{u}_i\}^T\{\bar{f}_i\}\,d\Gamma + L_i\left(\pm\frac{h}{2}\right)\int_S \{\tilde{u}_i\}^T\{\bar{p}_i^{\pm}\}\,dS\right]$$
$$+ \sum_{i,j=0}^{K}\left[\int_S \{\tilde{\eta}_i\}^T[E^t_{ij}]\{T_j\}\,dS + \int_{\Gamma_u} \{\tilde{u}_i\}^T[N][E^t_{ij}]\{T_j\}\,dS\right] \tag{16}$$

$$\sum_{i,j=0}^{K}\left[\int_S \{\tilde{T}_i\}^T[h_{ij}]\{\dot{T}_j\}\,dS + \int_S \{\tilde{\xi}_i\}^T[\ell_{ij}]\{\xi_j\}\,dS - \int_{\Gamma_T} \{\tilde{T}_i\}^T[N][\ell_{ij}]\{T_j\}\,d\Gamma\right]$$
$$= \sum_{i=0}^{K}\left[\int_{\Gamma_q} \{\tilde{T}_i\}^T\{\bar{q}_i\}\,d\Gamma + L_i\left(\pm\frac{h}{2}\right)\int_S \{\tilde{T}_i\}^T\{\bar{h}_i^{\pm}\}\,dS\right] \tag{17}$$

where

$$m_{ij} = \int_{-h/2}^{h/2} \rho L_i L_j\,dz \qquad [E^u_{ij}] = \int_{-h/2}^{h/2} [D^u] L_i L_j\,dz \qquad \{\bar{f}_i\} = \int_{-h/2}^{h/2} L_i(z)\{f\}\,dz$$
$$[E^t_{ij}] = \int_{-h/2}^{h/2} [D^t] L_i L_j\,dz \qquad h_{ij} = \int_{-h/2}^{h/2} \rho c L_i L_j\,dz$$
$$\ell_{ij} = \int_{-h/2}^{h/2} \kappa L_i L_j\,dz \qquad \bar{q}_i = \int_{-h/2}^{h/2} L_i(z)\hat{q}\,dz \tag{18}$$
$$[n] = \begin{bmatrix} n_x & 0 & 0 & 0 & n_z & n_y \\ 0 & n_y & 0 & n_z & 0 & n_x \\ 0 & 0 & n_z & n_y & n_x & 0 \end{bmatrix}$$

and n_x, n_y, and n_z are components of $\mathbf{n}$ along x, y, and z axes, respectively. Note that for $0 \le i,j \le K$, $[m_{ij}]$ is a $3(K+1)\times 3(K+1)$ matrix, $[E^u_{ij}]$ and $[E^t_{ij}]$ are $6(K+1)\times 6(K+1)$ and $6(K+1)\times(K+1)$ matrices, $[\ell_{ij}]$ and $[h_{ij}]$ are $(K+1)\times(K+1)$ matrices, and $[N]$ is a $3(K+1)\times 6(K+1)$ matrix derived from $[n]$. In the Galerkin formulation of the problem, $\{\tilde{u}_i\}$ and $\{\tilde{T}_i\}$ are usually taken to vanish on Γ_u and Γ_T, respectively. However, in the MLPG formulation, it is not necessary to do so since essential boundary conditions are imposed either by the penalty method or by the elimination of the corresponding degrees of freedom or by the method of Lagrange multipliers.

When ρ, c, κ, D^u, and D^t vary only through the thickness of the FG plate, then matrices m_{ij}, E^u_{ij}, E^t_{ij}, h_{ij}, and ℓ_{ij} are independent of the x and y coordinates.

IMPLEMENTATION OF THE MLPG METHOD

Semidiscrete Formulation

Let M nodes be placed on S, and $S_1, S_2, \ldots, S_M$ be smooth 2D closed regions enclosing nodes $1, 2, \ldots, M$ respectively such that $\cup_{\alpha=1}^{M} S_\alpha = S; S_1, S_2, \ldots, S_M$ need not be of the same shape and size, and the intersection of any two or more of them need not be empty. Let $\phi_1, \phi_2, \ldots, \phi_N$ and $\psi_1, \psi_2, \ldots, \psi_N$ be linearly independent functions defined on S_α. For a Kth-order plate theory there are $3(K+1)$ unknown displacements $\mathbf{u}_0, \mathbf{u}_1, \ldots, \mathbf{u}_K$ and $K+1$ unknown temperatures $T_0, T_1, \ldots, T_K$ at a point in S_α. We write these as $3(K+1)$- and $(K+1)$-dimensional arrays $\{u\}$ and $\{T\}$, respectively, and set

$$\{u(x,y,t)\} = \sum_{J=1}^{N} [\phi_J^u(x,y)]\{\delta_J(t)\} \qquad \{\tilde{u}(x,y)\} = \sum_{J=1}^{N} [\psi_J^u(x,y)]\{\tilde{\delta}_J\} \tag{19}$$

$$\{T(x,y,t)\} = \sum_{J=1}^{N} [\phi_J^t(x,y)]\{\tau_J(t)\} \qquad \{\tilde{T}(x,y)\} = \sum_{J=1}^{N} [\psi_J^t(x,y)]\{\tilde{\tau}_J\} \tag{20}$$

where, for each value of J, $\{\delta_J\}$ and $\{\tau_J\}$ are $3(K+1)$- and $(K+1)$-dimensional arrays, and $\{\phi_J^u\}$ and $[\phi_J^t]$ are square matrices of $3(K+1)$ and $(K+1)$ rows, respectively; similar remarks apply to $\{\tilde{u}\}, [\psi_J^u], \{\tilde{\delta}_J\}, \{\tilde{T}\}, [\psi_J^t]$, and $\{\tilde{\tau}_J\}$. Note that δ_J and τ_J vary with time t. The $3(K+1) \times 3(K+1)$ matrix $\{\phi_J^u\}$ and the $(K+1) \times (K+1)$ matrix $[\phi_J^t]$ can be divided into $K+1$ submatrices each of size $3 \times 3(K+1)$ and $1 \times (K+1)$, respectively. The ith submatrix of $[\phi_J^u]$ is given by

$$[i\text{th submatrix of } \phi_J^u] = \begin{bmatrix} \overbrace{0 & 0 & 0}^{0} & \ldots & \overbrace{\phi_J^u & 0 & 0}^{i} & \ldots & \overbrace{0 & 0 & 0}^{K} \\ 0 & 0 & 0 & \ldots & 0 & \phi_J^u & 0 & \ldots & 0 & 0 & 0 \\ 0 & 0 & 0 & \ldots & 0 & 0 & \phi_J^u & \ldots & 0 & 0 & 0 \end{bmatrix} \tag{21}$$

Note that the location of the 3×3 diagonal matrix $\phi_J^u I$, where I is a 3×3 unit matrix, depends on the value of i. For example, for $i = 0, \phi_J I$ occupies the first three rows and columns of $[\phi_J^u]$; for $i = 2$, the second three rows and columns, and so forth. The ith submatrix of $[\phi_J^t]$ is a $1 \times (K+1)$ matrix with ϕ_J^t in the ith column and zeros elsewhere. The analog of unknowns $\{\delta_J\}$ and $\{\tau_J\}$ are the nodal displacements and the nodal temperatures in the FEM. However, in the MLPG method, $\{\delta_J\}$ and $\{\tau_J\}$ do not generally equal nodal displacements and nodal temperatures, respectively. Substitution from Eqs. (19) and (20) into Eq. (11) gives

$$\{\eta\} = \sum_{J=1}^{N} [B_J^u]\{\delta_J\} \qquad \{\tilde{\eta}\} = \sum_{J=1}^{N} [\tilde{B}_J^u]\{\tilde{\delta}_J\} \qquad \{\xi\} = \sum_{J=1}^{N} [B_J^t]\{\tau\} \qquad \{\tilde{\xi}\} = \sum_{J=1}^{N} [\tilde{B}_J^t]\{\tilde{\tau}\} \tag{22}$$

where $\{\eta\}$ is a $6(K+1)$-dimensional array, $[B^u]$ is a $6(K+1)\times 3(K+1)$ matrix which can be divided into $(K+1)$ submatrices each of size $6\times 3(K+1)$, and $[B^t_J]$ is a $3(K+1)\times(K+1)$ matrix that can be divided into $(K+1)$ submatrices each of size $3\times(K+1)$. The ith such submatrices of $[B^u]$ and $[B^t]$ are given by

$$[i\text{th submatrix of } B^u_J] =$$

$$\begin{bmatrix}
\overbrace{0 & 0 & 0}^{0} & \dots & \overbrace{\partial\phi^u_J/\partial x & 0 & 0}^{i} & \dots & \overbrace{0 & 0 & 0}^{K} \\
0 & 0 & 0 & \dots & 0 & \partial\phi^u_J/\partial y & 0 & \dots & 0 & 0 & 0 \\
0 & 0 & \phi^u_J d_{0i} & \dots & 0 & 0 & \phi^u_J d_{ii} & \dots & 0 & 0 & \phi^u_J d_{Ki} \\
0 & \phi^u_J d_{0i} & 0 & \dots & 0 & \phi^u_J d_{ii} & \partial\phi^u_J/\partial y & \dots & 0 & \phi^u_J d_{Ki} & 0 \\
\phi^u_J d_{0i} & 0 & 0 & \dots & \phi^u_J d_{ii} & 0 & \partial\phi^u_J/\partial x & \dots & \phi^u_J d_{Ki} & 0 & 0 \\
0 & 0 & 0 & \dots & \partial\phi^u_J/\partial y & \partial\phi^u_J/\partial x & 0 & \dots & 0 & 0 & 0
\end{bmatrix} \tag{23}$$

$$[i\text{th submatrix of } B^t_J] = \begin{bmatrix}
\overbrace{0}^{0} & \dots & \overbrace{\partial\phi^t_J/\partial x}^{i} & \dots & \overbrace{0}^{K} \\
0 & \dots & \partial\phi^t_J/\partial y & \dots & 0 \\
\phi^t_J d_{0i} & \dots & \phi^t_J d_{ii} & \dots & \phi^t_J d_{Ki}
\end{bmatrix}$$

where the repeated index i in d_{ii} is not summed. The matrices $[\tilde{B}^u_J]$ and $[\tilde{B}^t_J]$ are obtained from $[B^u_J]$ and $[B^t_J]$ by substituting ψ^u_J for ϕ^u_J, and ψ^t_J for ϕ^t_J, respectively.

We now replace the domain of integration S in Eqs. (16) and (17) by S_α; substitute for $\{\eta\},\{\tilde{\eta}\},\{u\},\{\tilde{u}\},\{\xi\},\{\tilde{\xi}\},\{T\}$, and $\{\tilde{T}\}$ from Eqs. (19), (20), and (22); require that the resulting equation hold for all choices of $\{\tilde{\delta}\}$ and $\{\tilde{\tau}\}$; and arrive at the following system of coupled ordinary differential equations (ODEs):

$$\sum_{J=1}^{N}([K^u_{IJ}]\{\delta_J\}+[M^u_{IJ}]\{\ddot{\delta}_J\})=\{F^u_I\} \qquad \sum_{J=1}^{N}([K^t_{IJ}]\{\tau_J\}+[M^t_{IJ}]\{\dot{\tau}_J\})=\{F^t_I\} \tag{24}$$

where

$$\begin{aligned}
[K^u_{IJ}] = {} & \int_{S_\alpha}\left([\tilde{B}^u_I]^T[E^u][B^u_J]\right)dS-\int_{\Gamma_{\alpha u}}\left([\psi^u_I]^T[N][E^u][B^u_J]\right)d\Gamma \\
& -\int_{\Gamma_{\alpha 0}}\left([\psi^u_I]^T[N][E^u][B^u_J]\right)d\Gamma
\end{aligned}$$

$$\begin{aligned}
\{F^u_I\} = {} & \int_{\Gamma_{\alpha f}}[\psi_I]^T\{\bar{f}_i\}\,d\Gamma+L_i(\pm h/2)\int_{S_\alpha}[\psi_I]^T\{p^{\pm}\}\,dS \\
& +\sum_{J=1}^{N}\left[\int_S[\tilde{B}_I]^T[E^t][\phi^t_J]\{\tau_J\}\,dS-\int_{\Gamma_u}\{\psi^u_I\}^T[N][E^t]\{\phi^t_J\}\{\tau_J\}\,d\Gamma\right]
\end{aligned} \tag{25}$$

$$[M^u_{IJ}] = \int_{S_\alpha} [\psi^u_I]^T [m][\phi^u_J]\, dS \qquad [M^t_{IJ}] = \int_{S_\alpha} [\psi^t_I]^T [h][\phi^t_J]\, dS$$

$$[K^t_{IJ}] = \int_{S_\alpha} [\tilde{B}^t_J]^T [\ell][B^t_J]\, dS - \int_{\Gamma_{\alpha T}} \{\psi^t_I\}^T [N][\ell]\{\phi^t_J\} d\Gamma$$

$$\{F^t_I\} = \int_{\Gamma_{q\alpha}} \{\tilde{\psi}^t\}^T \{\bar{q}_i\}\, d\Gamma + L_i\left(\pm\frac{h}{2}\right) \int_{S_\alpha} \{\tilde{\psi}^t\}^T \{h^\pm\}\, dS$$

and where $\Gamma_{\alpha 0} = \partial S_\alpha - \Gamma_{\alpha u} - \Gamma_{\alpha f}, \Gamma_{\alpha u} = \partial S_\alpha \cap \Gamma_u, \Gamma_{\alpha f} = \partial S_\alpha \cap \Gamma_f$. The matrix $[K^u_{IJ}]$ is usually called the stiffness matrix, $[M^u_{IJ}]$ the mass matrix, $\{F^u_I\}$ the load vector, $[M^t]$ the heat capacity matrix, $[K^t]$ the thermal stiffness matrix, and $\{F^t\}$ the thermal load vector. For the MLPG formulation, $[M^u], [M^t], [K^u]$, and $[K^t]$ need not be symmetric and $[K^u]$ and $[K^t]$ may not be positive definite even after essential boundary conditions have been imposed. Equations like Eq. (24) are derived for each S_α ($\alpha = 1, 2, \ldots, M$). Initial conditions on $\{\delta_J\}$ and $\{\tau_J\}$ are obtained by substituting from Eqs. (19), (20), and (5) into Eq. (13) and following the procedure outlined after Eq. (13). For $\mathbf{u}^0 = \mathbf{0} = \dot{\mathbf{u}}^0$ and $T_0 = 0, \{\delta_J(0)\}, \{\dot{\delta}_J(0)\}$, and $\{\tau_J(0)\}$ are null matrices. Essential boundary conditions in Eq. (4) are satisfied by following the procedure outlined in the section Matrix Transformation Technique for Satisfying Essential Boundary Conditions.

In order to complete the formulation of the problem, we now describe briefly the moving least squares (MLS) approximation (see [42] for details) for finding basis functions $\{\phi_J\}$, and the technique to impose essential boundary conditions.

Brief Description of the MLS Basis Functions

In the MLS method, the approximation $f^h(x, y, t)$ of a scalar-valued function $f(x, y, t)$ defined on S_α is written as

$$f^h(x, y, t) = \sum_{j=1}^{m} p_j(x, y) a_j(x, y, t) \tag{26}$$

where

$$\mathbf{p}^T(x, y) = \{1, x, y, x^2, xy, y^2, \ldots\} \tag{27}$$

is a complete monomial in (x, y) having m terms. For complete monomials of degrees 1, 2, and 3, $m = 3$, 6, and 10, respectively. The unknown coefficients $a_1, a_2, \ldots, a_m$ are functions of $\mathbf{x} = (x, y)$ and time t, and are determined by minimizing R defined by

$$R = \sum_{i=1}^{n} W(\mathbf{x} - \mathbf{x}_i)[\mathbf{p}^T(\mathbf{x}_i)\mathbf{a}(\mathbf{x}, t) - \hat{f}_i(t)]^2 \tag{28}$$

where $\hat{f}_i(t)$ is the fictitious value at time t of f at the point (x_i, y_i), and n is the number of points in the domain of influence of $\mathbf{x}$ for which the weight function $W(\mathbf{x}-\mathbf{x}_i) > 0$. We take

$$W(\mathbf{x}-\mathbf{x}_i) = \begin{cases} 1 - 6\left(\frac{d_i}{r_w}\right)^2 + 8\left(\frac{d_i}{r_w}\right)^3 - 3\left(\frac{d_i}{r_w}\right)^4 & 0 \le d_i \le r_w \\ 0 & d_i \ge r_w \end{cases} \tag{29}$$

where $d_i = |\mathbf{x}-\mathbf{x}_i|$ is the distance between points $\mathbf{x}$ and $\mathbf{x}_i$, and r_w is the size of the support of the weight function W. Thus, the support of W is a circle of radius r_w with center at the point $\mathbf{x}_i$.

The stationarity of R with respect to $\mathbf{a}(\mathbf{x}, t)$ gives the following system of linear equations for the determination of $\mathbf{a}(\mathbf{x}, t)$:

$$\mathbf{A}(\mathbf{x})\mathbf{a}(\mathbf{x}, t) = \mathbf{B}(\mathbf{x})\hat{\mathbf{f}}(t) \tag{30}$$

where

$$\begin{aligned} \mathbf{A}(\mathbf{x}) &= \sum_{i=1}^{n} W(\mathbf{x}-\mathbf{x}_i)\mathbf{p}^T(\mathbf{x}_i)\mathbf{p}(\mathbf{x}_i) \\ \mathbf{B}(\mathbf{x}) &= [W(\mathbf{x}-\mathbf{x}_1)\mathbf{p}(\mathbf{x}_1),\ W(\mathbf{x}-\mathbf{x}_2)\mathbf{p}(\mathbf{x}_2), \ldots, W(\mathbf{x}-\mathbf{x}_n)\mathbf{p}(\mathbf{x}_n)] \end{aligned} \tag{31}$$

Substitution for $\mathbf{a}(\mathbf{x}, t)$ from Eq. (30) into Eq. (26) gives

$$f^h(\mathbf{x}, t) = \sum_{j=1}^{m} \phi_j(\mathbf{x})\hat{f}_j(t) \tag{32}$$

where

$$\phi_k(\mathbf{x}) = \sum_{j=1}^{m} p_j(\mathbf{x})[\mathbf{A}^{-1}(\mathbf{x})\mathbf{B}(\mathbf{x})]_{jk} \tag{33}$$

may be considered as the basis functions of the MLS approximation. It is clear that $\phi_k(x_j)$ need not equal the Kronecker delta δ_{kj}. In order for the matrix $\mathbf{A}$, defined by Eq. $(31)_1$, to be invertible, the number n of points in the domain of influence of $\mathbf{x}$ must at least equal m. For a 2D elastodynamic problem, Batra and Ching [43] used Gauss weight functions, the complete set of quadratic monomials, and $r_w = 3.5$ times the distance to the third node nearest to the node at $\mathbf{x}_i$. Thus, r_w and the locations of nodes in S_α and, hence, S must be such that n satisfies the required constraint. We take

$$r_w = s_f h_i \tag{34}$$

where h_i is the distance from node i to its nearest neighbor and s_f is a scaling parameter. We set $\psi_J = W(\mathbf{x} - \mathbf{x}_J)$ with $r_w = h_J$. Thus, the support of ψ_J is a circle centered at $\mathbf{x}_J$ and radius equal to the distance from $\mathbf{x}_J$ to the nearest node.

Matrix Transformation Technique for Satisfying Essential Boundary Conditions

We use the matrix transform technique to satisfy essential boundary conditions. In this subsection, the dependence on time is not explicitly indicated. Let D and I denote, respectively, the set of nodes where x displacements are and are not prescribed; a similar procedure is used for y and z displacements, and the thermal boundary condition. Writing the x displacements of all nodes as $\{u\}$, we have

$$\{u\} = \begin{Bmatrix} u_D \\ u_I \end{Bmatrix} = \begin{bmatrix} \phi_{DD} & \phi_{DI} \\ \phi_{ID} & \phi_{II} \end{bmatrix} \begin{Bmatrix} \delta_D \\ \delta_I \end{Bmatrix} \tag{35}$$

Solving the first of these equations for δ_D, we obtain

$$\{\delta\} = \begin{Bmatrix} \delta_D \\ \delta_I \end{Bmatrix} = \begin{Bmatrix} \phi_{DD}^{-1} u_D \\ 0 \end{Bmatrix} + \begin{bmatrix} -\phi_{DD}^{-1}\phi_{DI} \\ I \end{bmatrix} \{\delta_I\} \tag{36}$$

where 0 and I are the null and the identity matrices, respectively. Substitution from Eq. (36) into Eq. $(24)_1$ and the premultiplication of the resulting equation by

$$\begin{bmatrix} -\psi_{DD}^{-1}\psi_{DI} \\ I \end{bmatrix}^T$$

give

$$\sum_{J=1}^{N} ([\bar{K}_{IJ}^u]\{\delta_J\} + [\bar{M}_{IJ}^u]\{\ddot{\delta}_J\}) = \{\bar{F}_I^u\} \tag{37}$$

where

$$\begin{aligned}
[\bar{K}_{IJ}^u] &= \begin{bmatrix} -\psi_{DD}^{-1}\psi_{DI} \\ I \end{bmatrix}^T [K_{IJ}^u] \begin{bmatrix} -\phi_{DD}^{-1}\phi_{DI} \\ I \end{bmatrix} \\
[\bar{M}_{IJ}^u] &= \begin{bmatrix} -\psi_{DD}^{-1}\psi_{DI} \\ I \end{bmatrix}^T [M_{IJ}^u] \begin{bmatrix} -\phi_{DD}^{-1}\phi_{DI} \\ I \end{bmatrix} \\
\{\bar{F}_I^u\} &= \begin{bmatrix} -\psi_{DD}^{-1}\psi_{DI} \\ I \end{bmatrix}^T \{F_I^u\} - \begin{bmatrix} -\psi_{DD}^{-1}\psi_{DI} \\ I \end{bmatrix}^T [K_{IJ}^u] \begin{Bmatrix} \phi_{DD}^{-1} u_D \\ 0 \end{Bmatrix} \\
&\quad - \begin{bmatrix} -\psi_{DD}^{-1}\psi_{DI} \\ I \end{bmatrix}^T [M_{IJ}^u] \begin{Bmatrix} \phi_{DD}^{-1} \ddot{u}_D \\ 0 \end{Bmatrix}
\end{aligned} \tag{38}$$

Numerical Integration of ODEs

Equations $(24)_2$ are integrated for the ficticious nodal temperatures $\{\tau\}$ by the Crank–Nicolson or the central-difference method. Equations $(24)_1$ are then integrated with respect to time by the Newmark family of methods. In the Newmark family of methods, displacements $\boldsymbol{\delta}^{t+\Delta t}$ and velocities $\dot{\boldsymbol{\delta}}^{t+\Delta t}$ at time $t+\Delta t$ are related to their values at time t by

$$\begin{aligned}\boldsymbol{\delta}^{t+\Delta t} &= \boldsymbol{\delta}^t + \Delta t\dot{\boldsymbol{\delta}}^t + \frac{(\Delta t)^2}{2}((1-2\beta)\ddot{\boldsymbol{\delta}}^t + 2\beta\ddot{\boldsymbol{\delta}}^{t+\Delta t})\\ \dot{\boldsymbol{\delta}}^{t+\Delta t} &= \dot{\boldsymbol{\delta}}^t + \Delta t((1-\gamma)\ddot{\boldsymbol{\delta}}^t + \gamma\ddot{\boldsymbol{\delta}}^{t+\Delta t})\end{aligned} \tag{39}$$

where parameters β and γ control the accuracy and the stability of the integration scheme and Δt is the uniform time increment. The Newmark family of methods is unconditionally stable if

$$\gamma \geq \frac{1}{2} \quad \text{and} \quad \beta \geq \frac{1}{4}\left(\frac{1}{2}+\gamma\right)^2 \tag{40}$$

and second-order accurate for $\gamma = 1/2$ only; otherwise it is first-order accurate. Here we use $\gamma = 0.5$ and $\beta = 0.25$; thus, the integration scheme is unconditionally stable and nondissipative. However, the time-step size influences the accuracy of the computed solution.

ESTIMATION OF EFFECTIVE MATERIAL PROPERTIES

We assume that inclusions and the matrix are made of isotropic materials, inclusions are randomly distributed, and the macroscopic response of the composite can be modeled as isotropic. Vel and Batra [11] have shown that the Mori–Tanaka [6] and the self-consistent techniques [7] give different results for a simply supported FG plate loaded on the top surface. The emphasis here is to demonstrate the applicability of the HOSNDPT and the MLPG method to analyze transient thermoelastic problems for inhomogeneous bodies. Thus the use of a particular homogenization technique is less critical. We use the Mori–Tanaka method for its simplicity. It accounts approximately for the interaction among neighboring inclusions and is generally applicable to regions of the graded microstructure that have a well-defined continuous matrix and a discontinuous particulate phase.

Let subscripts 1 and 2 denote values of a quantity for phases 1 and 2, respectively. Thus, V_1 and $V_2 = 1 - V_1$ equal volume fractions of phases 1 and 2, respectively. The effective mass density, ρ, and the effective heat capacity, ρc, are given exactly by the rule of mixtures:

$$\rho = \rho_1 V_1 + \rho_2 V_2, \qquad \rho c = \rho_1 c_1 V_1 + \rho_2 c_2 V_2 \tag{41}$$

According to the Mori–Tanaka method [6], the effective shear modulus μ and the effective bulk modulus, $K = \lambda + 2\mu/3$, are given by

$$\begin{aligned} \frac{K - K_1}{K_2 - K_1} &= \frac{V_2}{1 + (1 - V_2)(K_2 - K_1)/(3K_1 + 4\mu_1)} \\ \frac{\mu - \mu_1}{\mu_2 - \mu_1} &= V_2 \Big/ \left(1 + (1 - V_2)\frac{(\mu_2 - \mu_1)}{(\mu_1 + f_1)}\right) \end{aligned} \tag{42}$$

where

$$f_1 = \mu_1(9K_1 + 8\mu_1)/(6(K_1 + 2\mu_1)) \tag{43}$$

The effective thermal conductivity κ [44] and the effective coefficient of thermal expansion α [45] are given by

$$\frac{\kappa - \kappa_1}{\kappa_2 - \kappa_1} = \frac{V_2}{1 + (1 - V_2)(\kappa_2 - \kappa_1)/3\kappa_1} \tag{44}$$

$$\frac{\alpha - \alpha_1}{\alpha_2 - \alpha_1} = \frac{1/K - 1/K_1}{1/K_2 - 1/K_1} \tag{45}$$

The through-the-thickness variation of V_2 is assumed to be given by

$$V_2 = V_2^- + (V_2^+ - V_2^-)\left(\frac{1}{2} + \frac{z}{h}\right)^p \tag{46}$$

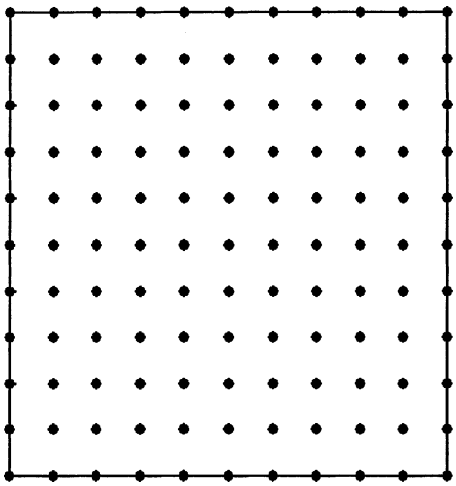

Figure 2. Thirteen uniformly spaced nodes in the x_1 and x_2 directions.

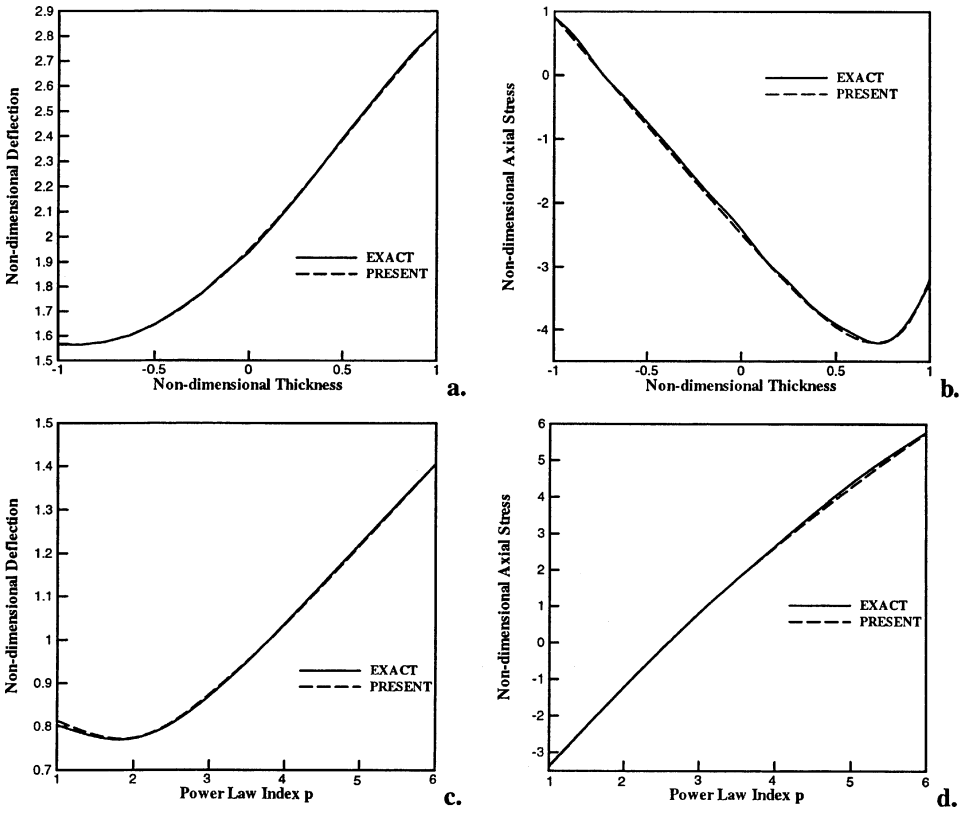

Figure 3. For the case of the steady heat conduction with the temperature prescribed on the top surface of the plate, comparison with the analytical solution [11] of the presently computed through-the-thickness variation of (*a*) the centroidal deflection and (*b*) the axial stress at the centroid of the top surface. Parts (*c*) and (*d*) compare the variation with the exponent p of the centroidal deflection and the axial stress at the centroid of the top surface.

where superscripts + and − signify, respectively, values of the quantity on the top and the bottom surfaces of the plate, and the parameter p describes the variation of phase 2; $p = 0$ and ∞ correspond to uniform distributions of phase 2 with volume fractions V_2^+ and V_2^-, respectively.

COMPUTATION AND DISCUSSION OF RESULTS

A computer code has been developed based on the aforestated MLPG formulation and the HOSNDPT. It has been validated by comparing the computed solution with the analytical results for elastostatic deformations, free and forced vibrations, and transient heat conduction in an FG plate. Here we analyze transient thermoelastic deformations of an FG plate. Vel and Batra [12] have recently given an analytical solution for transient heat conduction but quasi-static mechanical deformations of

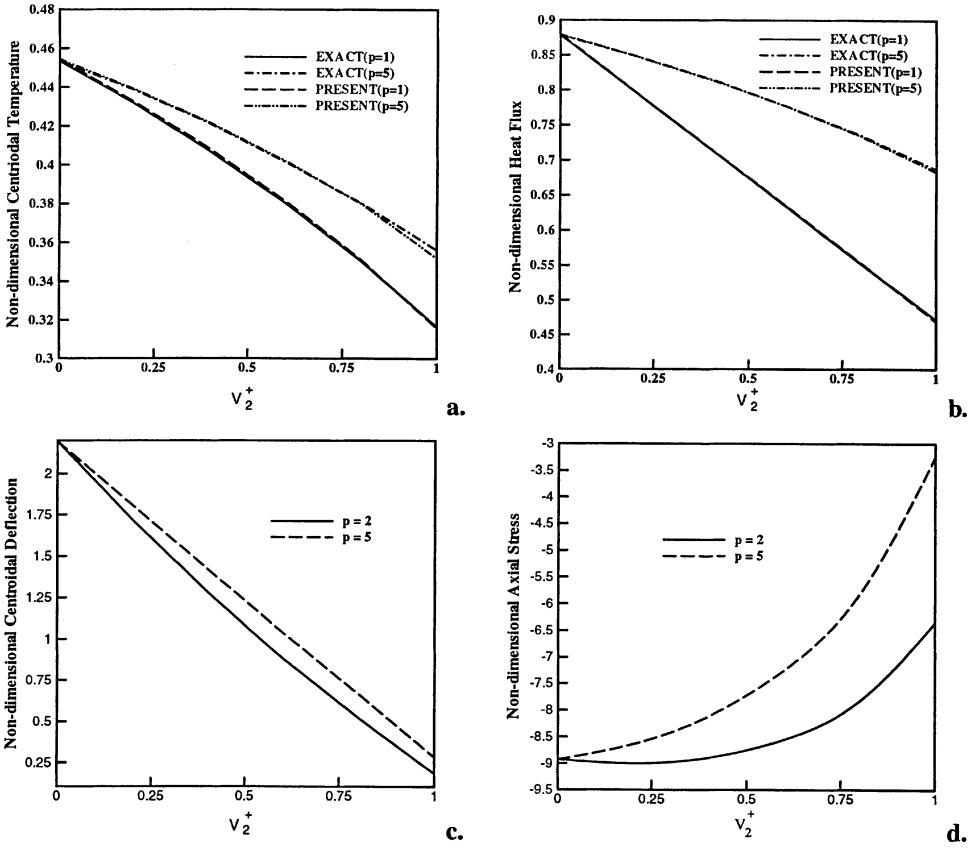

Figure 4. For the temperature prescribed on the top surface, comparison with the analytical solution of Vel and Batra [11] of the presently computed (*a*) centroidal temperature, and (*b*) heat flux at the centroid of the bottom surface. Parts (*c*) and (*d*) exhibit the variation with V_2^+ of the centroidal deflection and the axial stress at the centroid of the top surface.

an FG plate. We first compare our results with those of Vel and Batra, and then give results for transient thermomechanical deformations.

Boundary conditions imposed on the simply supported (S) and clamped (C) edges of an FG plate are

$$\begin{aligned} \text{S:}\quad & \sigma_{xx}=0 \quad v=w=0 \quad T=0 \quad \text{on } x=0,\ a \\ & \sigma_{yy}=0 \quad u=w=0 \quad T=0 \quad \text{on } y=0,\ b \end{aligned} \tag{47}$$

$$\text{C:}\quad u=v=w=T=0 \quad \text{on } x=0,\ a \qquad y=0,\ b$$

Hereafter we use S to denote a simply supported edge and not the midsurface of the plate. Equations $(47)_{1,2}$ do not simulate well boundary conditions encountered in a laboratory where rollers or sharp edges are used to support a plate. However,

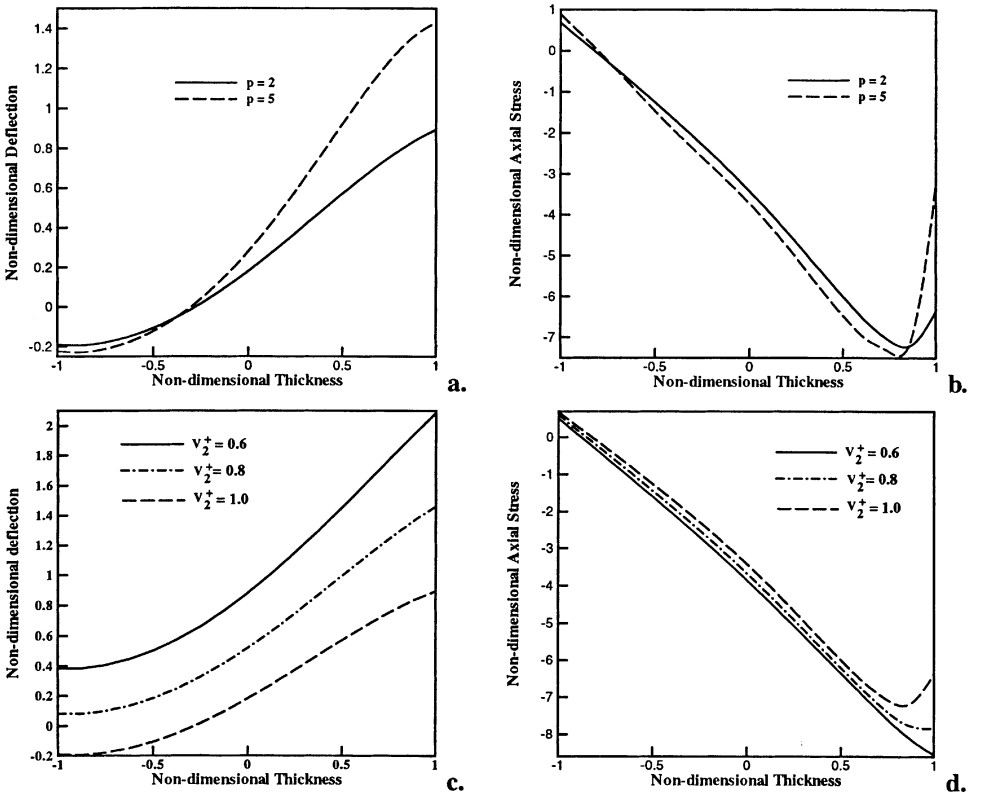

Figure 5. For temperature prescribed on the top surface of the plate, and for $p = 2$ and 5 through-the-thickness variation of (*a*) deflection and (*b*) the axial stress; corresponding results for $V_2^+ = 0.6,\ 0.8$, and 1.0 are depicted in (*c*) and (*d*).

analytical solutions are available for these boundary conditions. Batra and Geng [46, 47] have simulated the roller boundary conditions in their 3D FE analysis of large deformations of a hybrid piezoelectric plate.

Previous studies [23, 48, 49] of thick homogeneous and FG plates have indicated that a fifth-order shear and normal deformable plate theory (i.e., $K = 5$) and the following values of different variables in the MLPG formulation yield results that match very well with the analytical solution of the corresponding problem:

$$m = 15 \qquad s_f = 15 \qquad N = 13 \times 13 = 169 \qquad N_Q = 9 \times 9 = 81 \tag{48}$$

That is, fourth degree complete monomials are used to generate the MLS basis functions, 13 uniformly spaced nodes are used both in the x and the y directions (Figure 2), 81 quadrature points are employed to evaluate area integrals in Eq. (25), and 9 quadrature points are used to evaluate line integrals in Eq. (25). Thus, for a

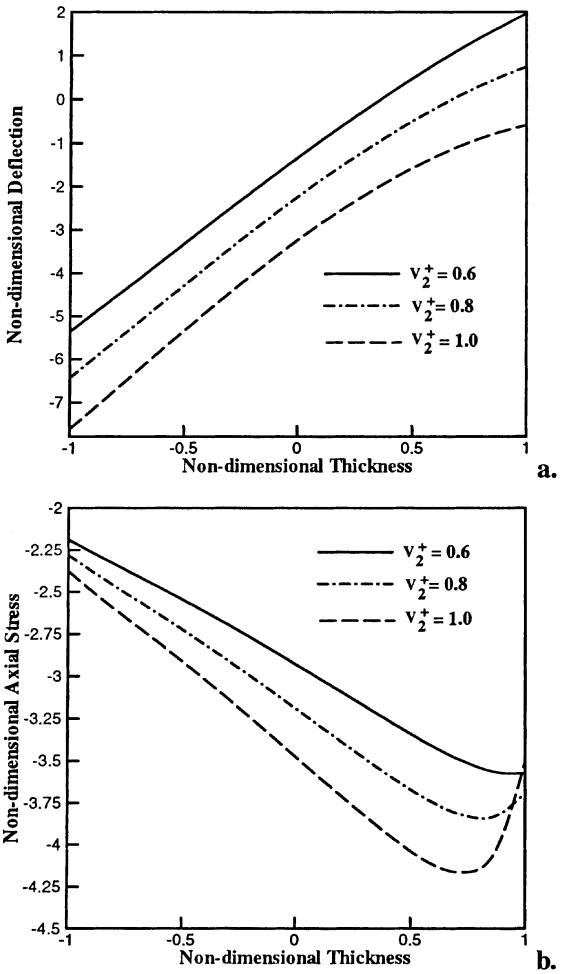

Figure 6. For heat flux prescribed on the top surface, and three values of V_2^+, through-the-thickness variation of (*a*) the centroidal deflection and (*b*) the axial stress on the centroidal axis.

free plate with temperature and displacements prescribed no where, the total number of degrees of freedom equals $4 \times 6 \times 169 = 4{,}056$.

For the square aluminum/silicon carbide FG plate of aspect ratio $h/a = 0.2$, the following values are assigned to material and geometric parameters:

$$
\begin{aligned}
& a = b = 250 \text{ mm} \qquad h = 50 \text{ mm} \\
\text{Al:}\quad & \rho_1 = 2707 \text{ kg/m}^3 \qquad c_1 = 896 \text{ J/kg K} \qquad \kappa = 233 \text{ W/mK} \\
& E_1 = 70 \text{ GPa} \qquad \nu_1 = 0.3 \qquad \alpha_1 = 23.4 \times 10^{-6}/\text{K} \\
\text{SiC:}\quad & \rho_2 = 3100 \text{ kg/m}^3 \qquad c_2 = 670 \text{ J/kg K} \qquad \kappa = 65 \text{ W/m K} \\
& E_2 = 427 \text{ GPa} \qquad \nu_2 = 0.17 \qquad \alpha_2 = 4.3 \times 10^{-6}/\text{K}
\end{aligned}
\tag{49}
$$

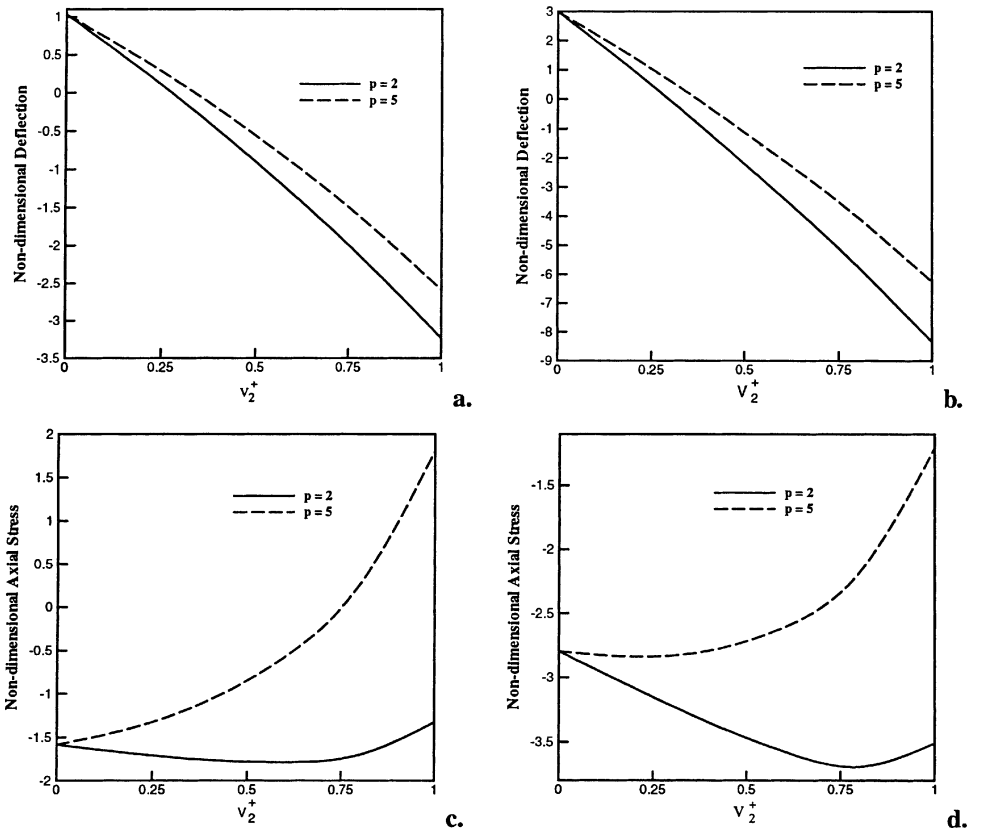

Figure 7. For $p = 2$ and 5, and heat flux prescribed on the top surface, variation with V_2^+ of the deflection of the centroids of (*a*) the top, (*b*) the bottom surfaces, and (*c*, *d*) the axial stress at these points.

Since the problem analyzed is linear, thermal and mechanical loads can be considered separately. Furthermore, a given load can be expanded in terms of Fourier series in the x and y directions. Thus, it suffices to consider the following spatial variation of the thermal loads on the top and the bottom surfaces of the plate. The thermal load increases exponentially in time to its steady-state value.

a. Temperature prescribed on the major surfaces of the plate:

$$\begin{aligned} T(x,y,h/2,t) &= T_0^+(1-e^{-\gamma t})\sin\frac{\pi x}{a}\sin\frac{\pi y}{b} \qquad \text{on } z = h/2 \\ T(x,y,-h/2,t) &= 0 \qquad \text{on } z = -h/2 \end{aligned} \tag{50}$$

Results are presented in terms of following nondimensional variables:

$$\bar{T} = \frac{T}{T_0^+} \qquad \bar{q} = -\frac{qh}{\kappa_1 T_0^+} \qquad \bar{w} = \frac{100hw}{\alpha_1 T_0^+ a^2} \qquad \bar{\sigma}_{xx} = \frac{10\sigma_{xx}}{E_1\alpha_1 T_0^+} \tag{51}$$

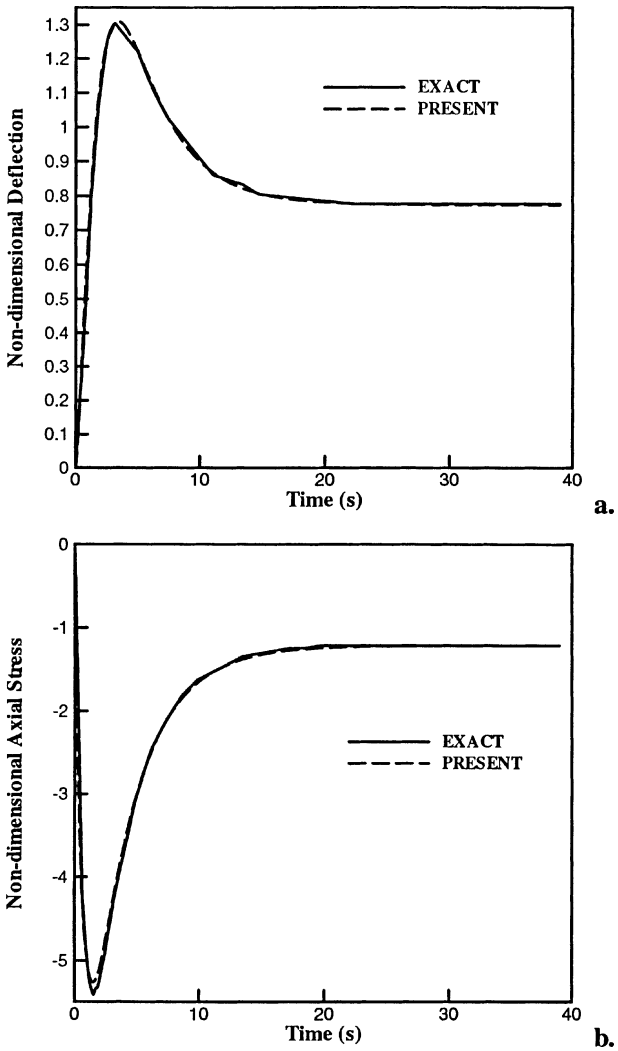

Figure 8. For $V_2^+ = 1.0$, $p = 2$, $\gamma = 1/s$, and temperature prescribed on the top surface of the plate, comparison of the presently computed time histories of the centroidal deflection and the axial stress at the plate centroid with those obtained from the analytical solution of Vel and Batra [12].

The reference length and the reference stress nondimensionalizing displacements and stresses, respectively, equal the axial elongation of a free aluminum bar of length a and magnitude of the axial stress induced in this bar clamped at the edges caused by the temperature rise of T^+. For aluminum and $T_0^+ = 100\,K$, these quantities respectively equal 0.585 mm and 63.8 MPa.

b. Heat flux prescribed on major surfaces of the plate:

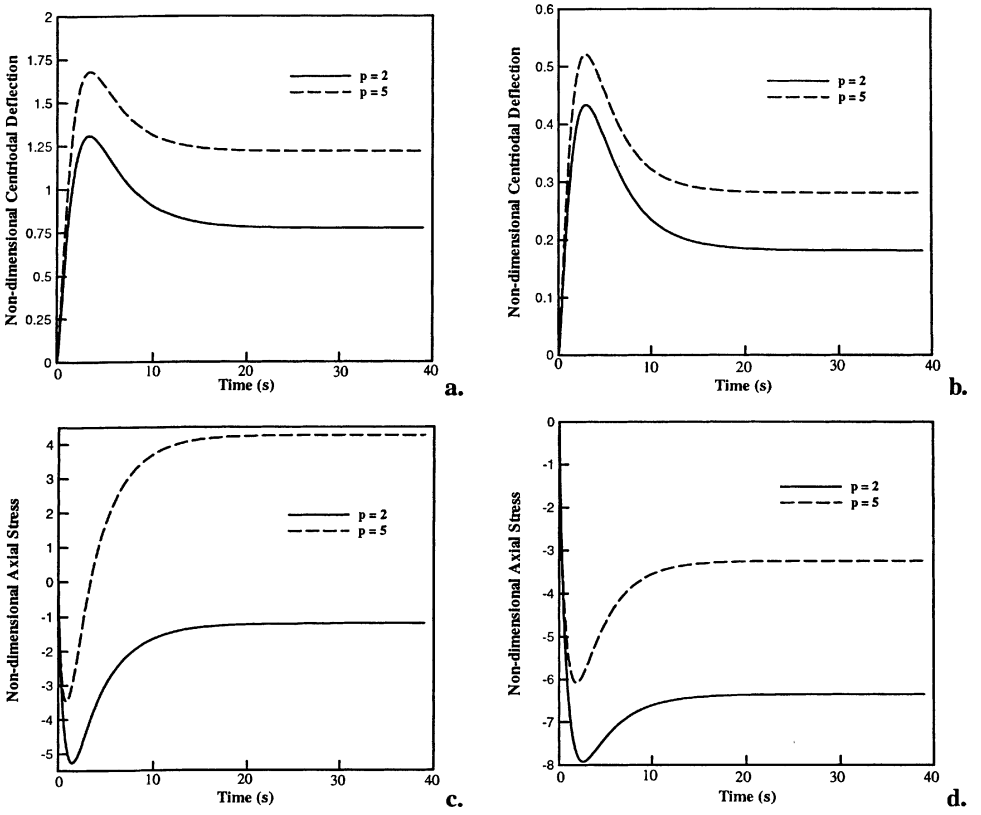

Figure 9. For $V_2^+ = 1.0$, $\gamma = 1/\text{s}$, $p = 2$ and 5, and temperature prescribed on the top surface of the plate time histories of the centroidal deflection for (*a*) simply supported and (*b*) clamped edges; the axial stress at the centroid of the top surface for the two types of boundary conditions is depicted in (*c*) and (*d*).

$$\begin{aligned} q_3(x, y, h/2, t) &= q_0^+(1 - e^{-\gamma t}) \sin\frac{\pi x}{a} \sin\frac{\pi y}{b} \qquad \text{on } z = h/2 \\ q_3(x, y, -h/2, t) &= 0 \qquad \text{on } z = -h/2 \end{aligned} \tag{52}$$

In the figures, the following nondimensional variables are used:

$$\bar{T} = \frac{Tk_1}{q_0^+ h} \qquad \bar{w} = \frac{100\kappa_1 w}{\alpha_1 q_0^+ a^2} \qquad \bar{\sigma}_{xx} = \frac{10\kappa_1 \sigma_{xx}}{E_1 \alpha_1 a q_0^+} \tag{53}$$

Thus, the reference value of the temperature equals the temperature difference across an aluminum bar of length h caused by the steady-state heat flux of q^+ through it. The reference values of the displacement and the stress equal the elongation of a free bar of length a and the magnitude of the axial stress developed in such a clamped bar with the heat flux q_0^+ applied across the faces. For $q_0^+ = 10^6$ W/m^2, a value typical

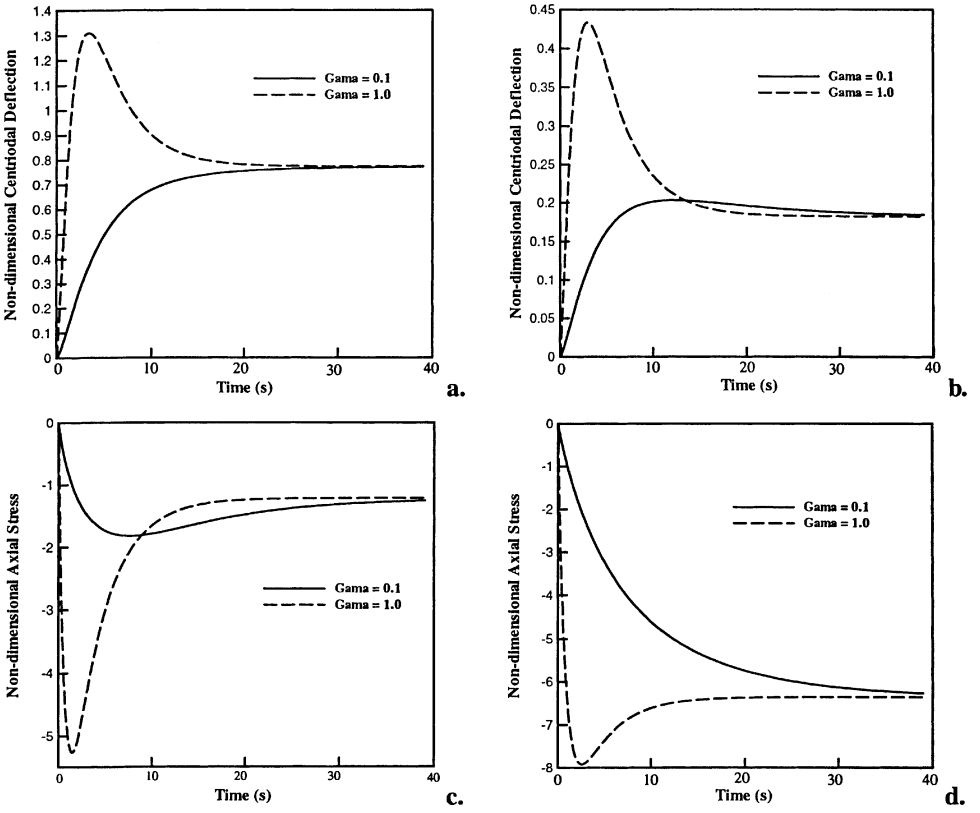

Figure 10. For $V_2^+ = 1.0$, $p = 2$, $\gamma = 0.1/\text{s}$, and $1.0/\text{s}$, and temperature prescribed on the top surface of the plate, time histories of the centroidal deflection for (*a*) simply supported and (*b*) clamped edges; the axial stress at the centroid of the top surface for the two types of boundary conditions is depicted in (*c*) and (*d*).

for laser heating, the reference temperature, displacement, and stress equal, respectively, 214.6 K, 6.28 mm, and 176 MPa.

Steady-State Heat Conduction

Temperature prescribed on the top surface. Results from the present method are compared with those from the analytical solution of Vel and Batra [11] in Figures 3*a*–3*d*. It is clear that the two sets of values of through-the-thickness variations of the centroidal deflection and the axial stress match with each other. Also, variations, with the exponent p in Eq. (46), of the centroidal deflection and the axial stress at the centroid of the top surface computed from the present method match very well with those obtained analytically [11]. The transverse displacement of the centroid of the top surface is nearly twice that of the centroid of the bottom surface, signifying an average transverse normal strain of 731×10^{-6} for $T^+ = 100$ K, and is proportional to $(a/h)^2$. The magnitude of the maximum compressive stress induced in the plate occurs at a point near the bottom surface of the plate and equals nearly nine times

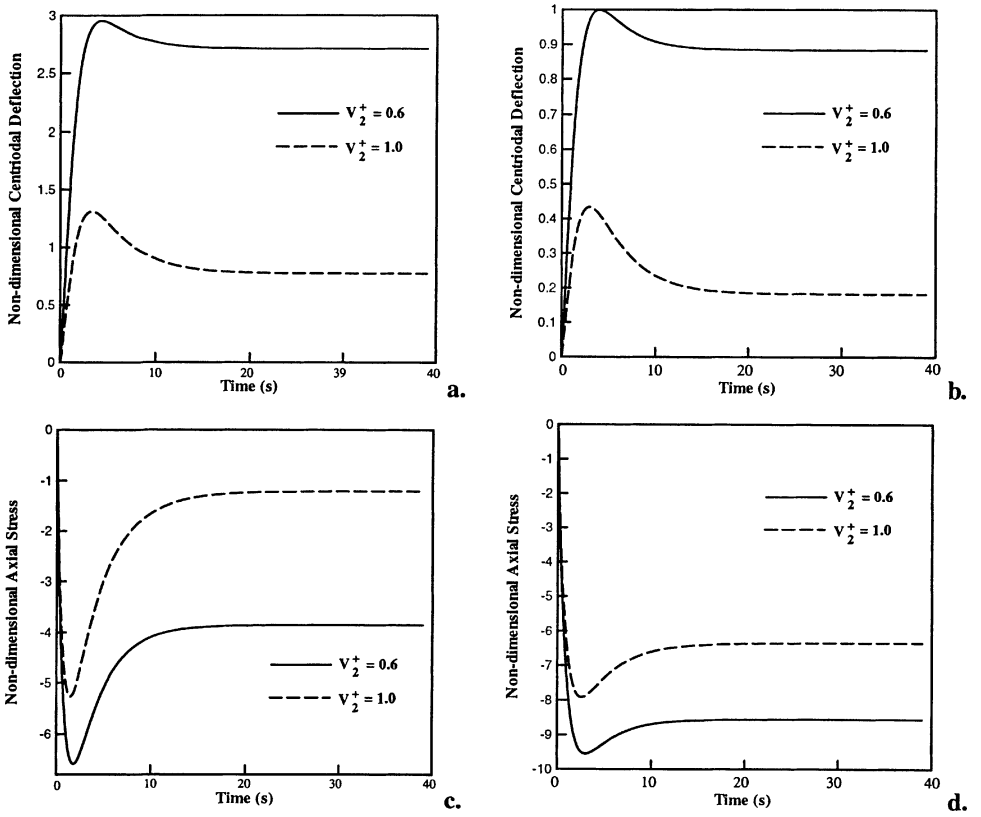

Figure 11. For $\gamma = 1/\text{s}$, $p = 2$, and $V_2^+ = 0.6$ and 1.0, and temperature prescribed on the top surface of the plate, time histories of the centroidal deflection for (*a*) simply supported and (*b*) clamped edges; the axial stress at the centroid of the top surface for the two types of boundary conditions is depicted in (*c*) and (*d*).

the tensile axial stress at the centroid of the top surface of the plate. An increase in the value of p in Eq. (46) results in a lower value of the volume fraction of SiC at a point. Results of Figure 3*c* imply that the centroidal deflection increases with an increase in the value of p, and the nondimensional axial stress at the top surface of the plate changes from -3.5 for $p = 1$ to 5.8 for $p = 6$. Results plotted in Figures 4*a* and 4*b* evince that the centroidal temperature and the heat flux at the centroid of the bottom surface computed by the two methods for various values of V_2^+ and the exponent p match very well. For $p = 2$ and 5, Figures 4*c* and 4*d* evince the variation with V_2^+ of the centroidal deflection and the axial stress at the centroid of the top surface. Because of the lower thermal conductivity of SiC, a higher value of V_2^+ results in a lower value of the centroidal temperature and the centroidal heat flux in the transverse direction. Also, the transverse displacement of the plate centroid decreases with an increase in the value of V_2^+ but the magnitude of the axial compressive stress induced at the centroid of the top surface decreases with an increase in V_2^+. The effect of varying p from 2 to 5 is less noticeable in the centroidal deflection than in the centroidal temperature, the transverse deflection of the plate centroid and

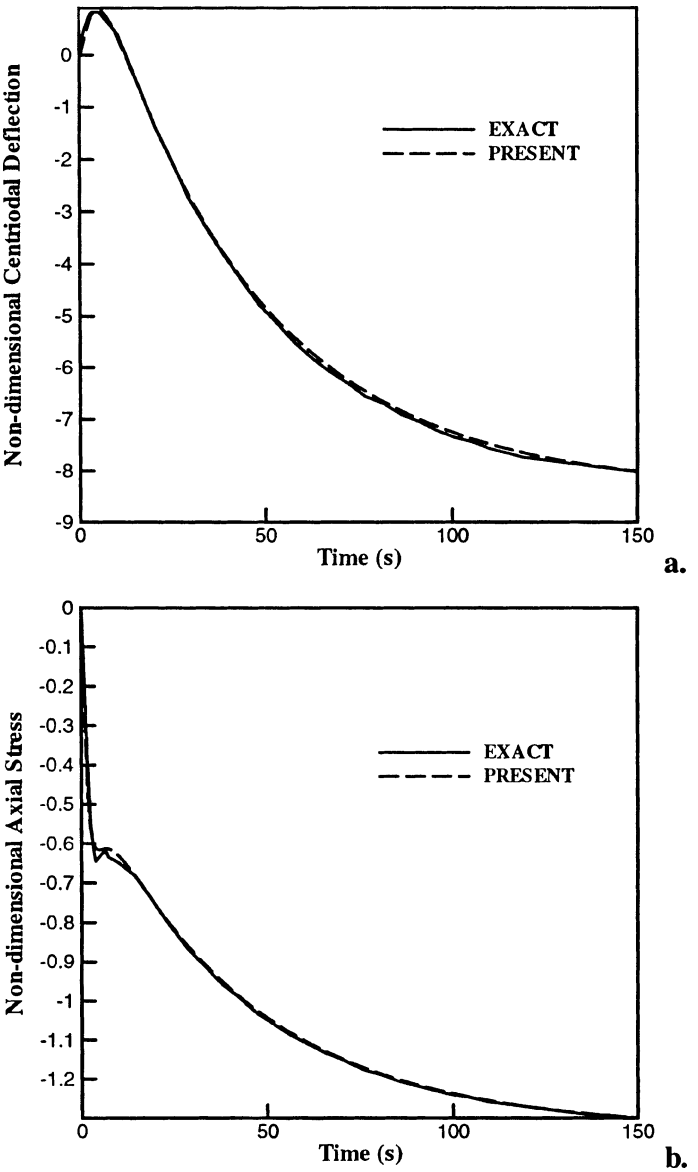

Figure 12. For $V_2^+ = 1.0$, $p = 2$, $\gamma = 1.0/\text{s}$, and heat flux prescribed on the top surface of the plate, comparison of the presently computed time histories of (*a*) the centroidal deflection and (*b*) the axial stress at the plate centroid with those from the analytical solution of Vel and Batra [12].

the axial stress at the centroid of the top surface of the plate. For $p = 2$ and 5, and $V_2^+ = 0.6,\ 0.8$, and 1.0, Figures 5*a*–5*d* depict through-the-thickness variations on the centroidal axis of the deflection and the axial stress. It is evident from the results of Figures 5*a* and 5*c* that the average transverse normal strain is higher for $p = 5$ than

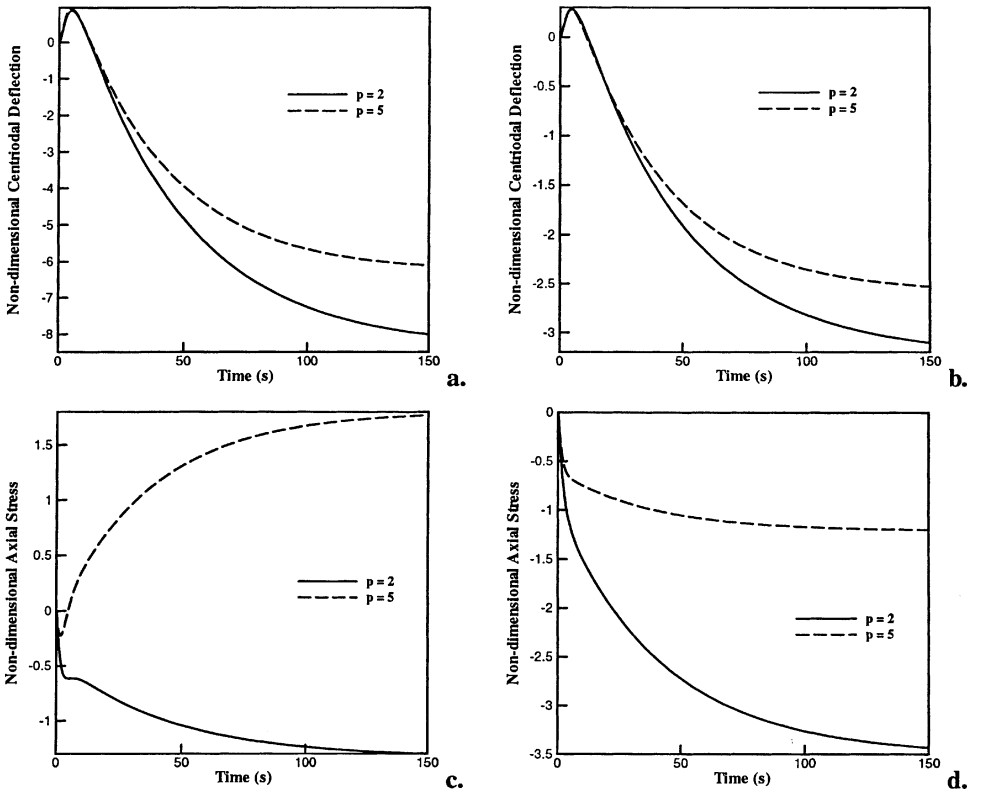

Figure 13. For $V_2^+ = 1.0$, $\gamma = 1/\text{s}$, $p = 2$ and 5, and heat flux prescribed on the top surface of the FG plate, time histories of the centroidal deflection for (*a*) simply supported and (*b*) clamped edges; the axial stress at the centroid of the top surface for the two types of boundary conditions is depicted in (*c*) and (*d*).

that for $p = 2$ and increases with a decrease in the value of V_2^+. Changing p from 2 to 5 affects more the axial stress induced at centroids of horizontal planes near the top surface of the plate. A similar effect is noticed when V_2^+ is varied from 0.6 to 1.0. It should be noted that the thermal stresses are induced by the temperature gradient and are also affected by the stress–temperature modulus.

Heat flux prescribed on the top surface. In Figures 6*a* and 6*b*, we have plotted through-the-thickness variation of the centroidal deflection and the axial stress on the centroidal axis of the plate for $V_2^+ = 0.6,\ 0.8$, and 1.0. For the same change in V_2^+, the decrease in the magnitude of the deflection near the top surface is more than that near the bottom surface of the plate. For each value of V_2^+, through-the-thickness variation of the deflection near the bottom surface of the plate is almost affine but that near the top surface is parabolic. The point where the magnitude of the axial stress is a maximum shifts toward the plate centroid with an increase in the value of V_2^+. The effect of changing V_2^+ is greater on the maximum magnitude of the axial stress than that on the magnitude of the axial stress at the centroid of either

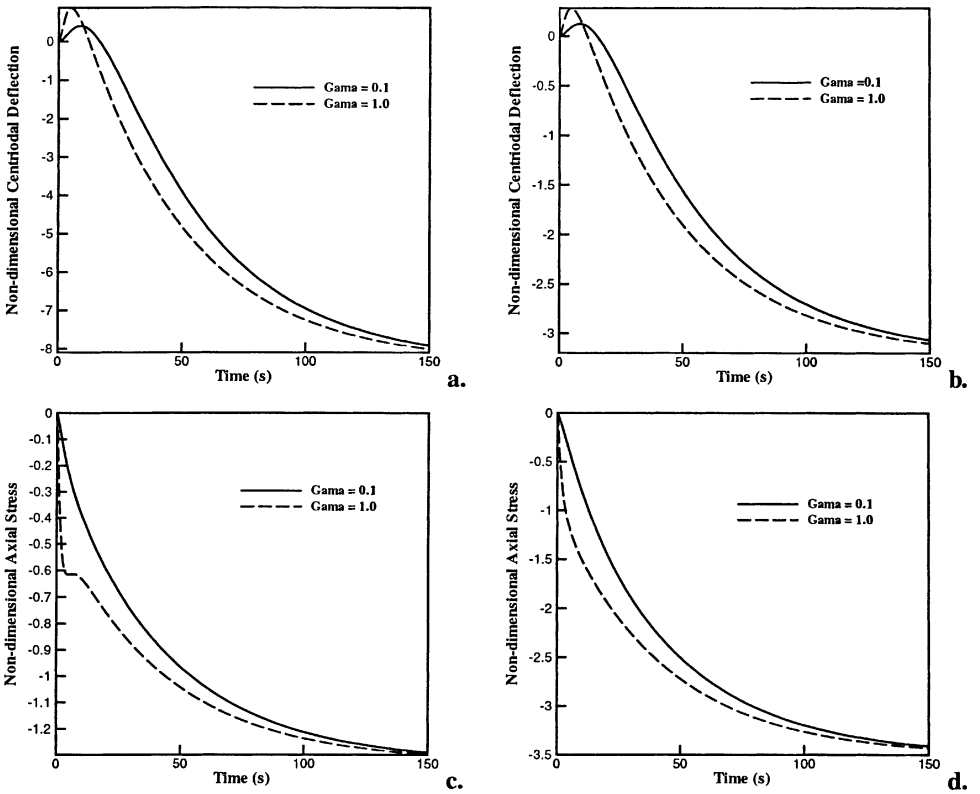

Figure 14. For $V_2^+ = 1.0$, $p = 2$, $\gamma = 0.1/\text{s}$ and $1.0/\text{s}$, and heat flux prescribed on the top surface of the plate, time histories of the centroidal deflection for (*a*) simply supported and (*b*) clamped edges; the axial stress at the centroid of the top surface for the two types of boundary conditions is depicted in (*c*) and (*d*).

the top or the bottom surfaces of the plate. The variations with V_2^+ of the deflection of the centroids of the top and the bottom surfaces, and of the axial stress at these points, are depicted in Figures 7*a*–7*d*. The most noticeable effect of changing p from 2 to 5 is on the magnitudes of the axial stress at the centroids of the top and bottom surfaces of the plate. For $V_2^+ = 1.0$ the nondimensional axial stress at the centroid of the top surface changes from 1.75 to -1.5 when p is increased from 2 to 5; that at the centroid of the bottom surface goes from -1.2 to -3.5. For $p = 5$, the axial stress at the centroid of the top surface changes parabolically from -1.4 to 1.75 as V_2^+ is increased from 0 to 1, and that at the centroid of the bottom surface remains essentially constant at -2.8 for $0 \leq V_2^+ \leq 0.25$ and then varies parabolically to -1.2 for $V_2^+ = 1.0$. The qualitative nature of the dependence on V_2^+ of the deflections of the centroids of the top and bottom surfaces is the same; however, for $p = 2$ the deflection of the centroid of the top surface goes from 1 for $V_2^+ = 0$ to -3.2 for $V_2^+ = 1.0$ but that of the centroid of the bottom surface changes from 3.0 for $V_2^+ = 0$ to -8.5 for $V_2^+ = 1.0$. Thus, the average transverse normal strain induced in the plate is more for $V_2^+ = 1.0$ than that for $V_2^+ = 0.0$.

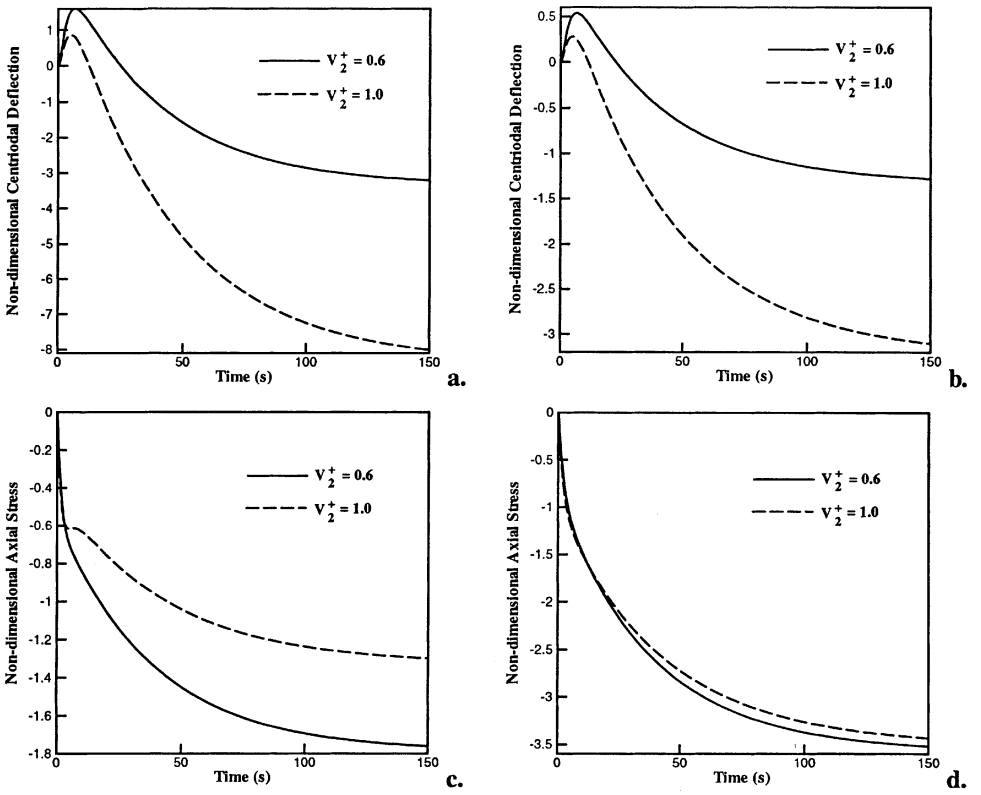

Figure 15. For $\gamma = 1/\text{s}$, $p = 2$, and $V_2^+ = 0.6$ and 1.0, and heat flux prescribed on the top surface of the plate, time histories of the centroidal deflection for (*a*) simply supported and (*b*) clamped edges; the axial stress at the centroid of the top surface for the two types of boundary conditions is depicted in (*c*) and (*d*).

Transient Heat Conduction

Results presented in this section are without the effects of inertia forces: quasi-static mechanical problems with transient heat conduction are analyzed.

Temperature prescribed on the top surface. For $V_2^+ = 1.0$, $p = 2$, and $\gamma = 1/\text{s}$, we have compared in Figures 8*a* and 8*b* the presently computed time histories of the centroidal deflection and the axial stress at the plate centroid with those of the analytical solution of Vel and Batra [12]. It is clear that the two sets of results agree with each other. Note that the peak centroidal deflection is nearly 50% more than the steady-state value and the maximum magnitude of the axial stress is four times its steady-state value. For $\gamma = 1/\text{s}$ the magnitude of the axial stress at the plate centroid reaches its peak value at $t \simeq 1.5\,\text{s}$ but the centroidal deflection becomes maximum at $t \simeq 3.0\,\text{s}$. For $p = 2$ and 5 we have plotted in Figures 9*a* and 9*b* the time history of the centroidal deflection for an FG plate with simply supported and clamped edges. These plots show that the qualitative nature of results is unaffected by the edge conditions. However, the peak centroidal deflection for the clamped edges is nearly

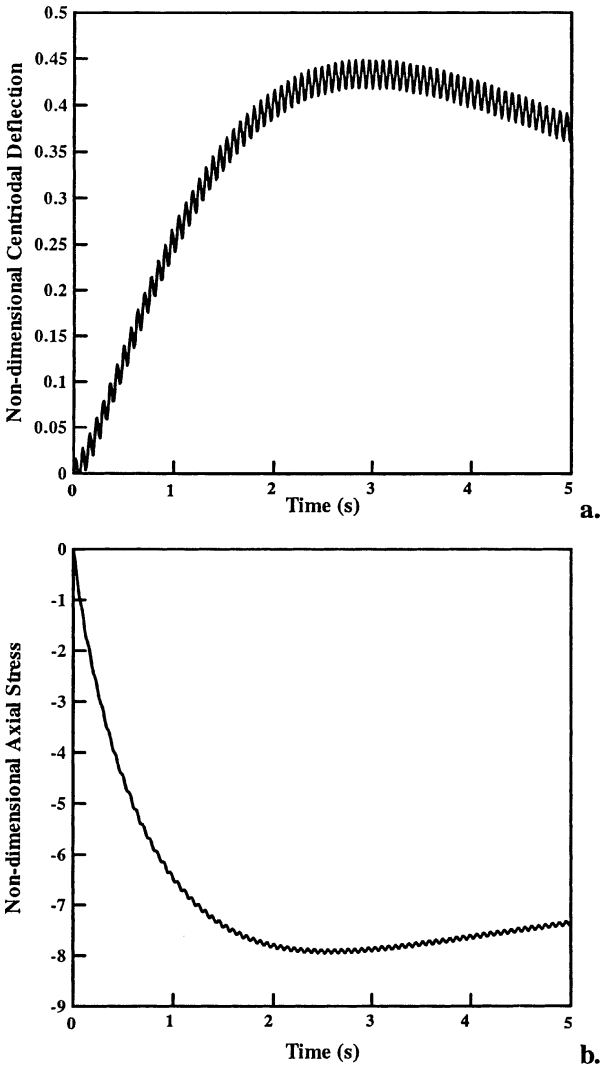

Figure 16. For a clamped FG plate subject to a transient temperature and an oscillatory pressure field on the top surface only, time history of (*a*) the centroidal deflection, and (*b*) the axial stress at the centroid of the top surface.

one-third of that for the case of simply supported edges. For a clamped FG plate the peak centroidal deflection is nearly 2.2 times the steady-state value, and for a simply supported FG plate this ratio is about 1.5. The time histories of the axial stress at the top surface of the plate centroid plotted in Figures 9*c* and 9*d* reveal that the steady-state value will give an incorrect estimate of the magnitude and the sign of the peak axial stress. For a simply supported plate, and $p = 5$, the steady-state value of the nondimensional axial stress equals about 4 but is compressive when plate deformations are varying with time; the magnitude of the maximum compressive

stress equals 3.5. For the clamped FG plate, the axial stress stays compressive and the ratio of the steady-state value to the peak value equals 0.8 and 0.55 for $p = 2$ and 5, respectively. For $p = 2$, the maximum compressive axial stress induced in the clamped FG plate is nearly 50% more than that in a simply supported plate.

The effect of the rate of increase of the prescribed temperature on the centroidal deflection and the axial stress at the centroid of the top surface of the plate is exhibited in Figures 10*a*–10*d*. For $\gamma = 0.1/\text{s}$, it takes 10 times longer for the prescribed temperature on the top surface to reach a certain value as compared to that for $\gamma = 1.0/\text{s}$. Results plotted in Figure 10 evince that the peak centroidal deflection and the maximum compressive stress induced at the centroid of the top surface of the plate are considerably higher for $\gamma = 1.0/\text{s}$ than those for $\gamma = 0.1/\text{s}$. The qualitative nature of these results is not affected by the edge conditions. Also, the steady-state values are the same for $\gamma = 0.1$, and 1.0, as should be the case. Thus, increasing the temperature suddenly will induce a considerably higher compressive axial stress than if the temperature were gradually increased to the steady-state value. For $p = 2, \gamma = 1.0/\text{s}$ and $V_2^+ = 0.6$ and 1.0, we have plotted in Figures 11*a*–11*d* the centroidal deflection and the axial stress at the centroid of the top surface of the plate for simply supported and clamped FG plates. For both types of edge conditions, a higher value of V_2^+ gives a lower value of the centroidal deflection and also of the maximum compressive stress induced at the centroid of the top surface of the FG plate.

Heat flux prescribed on the top surface. We have compared in Figures 12*a* and 12*b* the computed time histories of the centroidal deflection and the axial stress at the centroid of the top surface of a simply supported plate with those from the analytical solution of Vel and Batra [12]. The two sets of results virtually overlap each other. A comparison of these results with those given in Figure 8 reveals that it takes much longer for the centroidal deflection and the axial stress to reach their steady-state values when heat flux is prescribed on the top surface than when the temperature is assigned, even though both have the same rate of growth. For the case of the prescribed heat flux, the magnitude of axial stress at the plate centroid continues to increase very rapidly in the beginning and then gradually until the computational time of 150 s. However, when the temperature is prescribed on the top surface, the magnitude of the axial stress at the plate centroid increases quickly to its peak value, then gradually decreases and approaches steady value at $t \simeq 15$ s. As for the case of the temperature prescribed on the top surface of the plate, results plotted in Figures 13*a* and 13*b* reveal that the time histories of the centroidal deflection for a simply supported and a clamped plate look similar; however, the centroidal deflection at $t = 150$ s for a clamped FG plate is about 37% of that for a simply supported plate. Both for a clamped and a simply supported FG plate, the initial centroidal deflection is in a direction opposite to that of the final deflection. The through-the-thickness variation of the volume fraction of SiC, as specified by the value of p, has a noticeable effect on the time history of the axial stress at the centroid of the top surface of the plate. For a simply supported FG plate, the axial stress is positive for $p = 2$, and increases monotonically to its steady-state value, but is negative for $p = 5$. For a clamped plate, the axial stress has the same sign for $p = 2$ and 5. The

steady-state value of the axial stress for $p = 2$ is nearly four times that for $p = 5$. Comparison of results plotted in Figures 9 and 13 suggests that the qualitative nature of the time histories of the centroidal deflection for simply supported and clamped plates is the same whether the transient heat flux or the transient temperature is prescribed on the top surface of the plate. However, the time histories of the axial stress at the centroid of the top surface differ both qualitatively and quantitatively.

A comparison of results plotted in Figures 14*a* and 14*b* with those in Figures 10*a* and 10*b* reveals that the value of γ has a minor effect on the centroidal deflection when heat flux is prescribed on the top surface than when the temperature is specified. Also, the time histories of the centroidal deflection for the two types of edge conditions are quite similar. As for the centroidal deflection, the axial stress at the centroid of the top surface of the plate is less influenced by the value of γ than was the case with the temperature prescribed on the top surface. Also, the axial stress and the centroidal deflection approach their steady-state values considerably slowly in the case of the heat flux prescribed on the top surface. The effect of changing V_2^+ from 0.6 to 1.0 on the time histories of the centroidal deflection and the axial stress at the centroid of the top surface of the plate is exhibited in Figures 15*a*–15*d*. The time histories are qualitatively similar for simply supported and clamped plates. At $t = 150$ s the centroidal deflection for $V_2^+ = 0.6$ is nearly one-fourth of that for $V_2^+ = 1.0$ for both simply supported and clamped FG plates. Whereas the value of V_2^+ strongly influences the steady-state axial stress induced at the centroid of the top surface of a simply supported plate, it has very little effect for a clamped plate.

Transient Heat Conduction with the Consideration of Inertia Forces

Both for a simply supported and a clamped plate, and for either transient temperature or transient heat flux prescribed on the top surface of the plate, the computed time histories of the centroidal deflection and the axial stress at the centroid of the top surface of the plate were unaffected by the consideration of inertia forces. It is because accelerations induced by the temperature gradients are negligible. Moreover, results computed with and without the consideration of inertia forces for $h/a = 0.025$, 0.05, 0.1, and 0.2 were identical to each other.

Combined Transient Thermal and Mechanical Loads

We now study transient thermomechanical deformations of a clamped FG plate with $V_2^+ = 1.0, V_2^- = 0.0, T^+ = 100$ K, $\gamma = 1/$s, and $p = 2$. The thermal load consists of the temperature prescribed on the top surface of the plate and the mechanical load is a normal pressure on the top surface given by

$$200 \sin \omega t \sin \frac{\pi x}{a} \sin \frac{\pi y}{b} \text{ kN/m}^2$$

with $\omega = 60$ rad/s and the bottom surface kept traction free. Figures 16*a* and 16*b* depict, respectively, the time history of the centroidal deflection and the axial stress

at the centroid of the top surface of the plate. The oscillations in the centroidal deflection are due to the oscillatory nature of the mechanical load. Under a pure oscillatory mechanical load, the plate will vibrate with the frequency of the applied load. The increase in the magnitude of the axial stress and the centroidal deflection is due to the transient thermal load. The centroidal deflection oscillates around the value determined by the thermal load.

In contrast to the HOSNDPT used here, Qian et al. [50] have used the MLPG method to seek an approximate solution of equations governing the coupled static thermoelastic deformations of an FG plate. Furthermore, they [51] have used the MLPG method and the HOSNDPT to find the spatia compositional profile in an FG plate with the volume fractions of constituents varying both in the x- and the z-directions so as to optimize the first or the second natural frequency of a clamped rectangular plate. Batra and Love [52] have employed the FEM to study the initiation and propagation of adiabatic shear bands in a FG plate made of tungsten and nickel-iron with their volume fractions varying in two directions. It involves seeking a numerical solution of a transient coupled thermomechanical problem for a thermo-elasto-viscoplastic body. Whereas in all these problems effective material moduli of the homogenized body were used, Batra et al. [53] have shown that the methods of Lagrange multipliers and a jump function introduced by Krongauz and Belytschko [54] can be used in conjuction with the MLPG method to study transient heat conduction in a bimetallic disk. These techniques satisfactorily account for the jump in the normal derivative to temperature to ensure that the heat flux at the interface between two different materials is continuous. For an anisotropic FG graphite/epoxy rectangular plate with fiber orientation varying continuously through the plate thickness, Batra and Jin [55] have scrutinized the dependence of first few natural frequencies upon through-the-thickness variation of the fiber orientation. Instead of the MLPG method used here, one could also use the modified smoothed particle hydrodynamics (MSPH) method to analyze the transient coupled thermomechanical deformations of a plate; e.g. see [56,57].

CONCLUSIONS

We have analyzed transient thermomechanical deformations of an FG thick plate loaded by either a thermal load or a combined thermal and mechanical load on the top surface. The edges of the plate may be either simply supported or clamped. The problem is studied by using an HOSNDPT and an MLPG method. For the case of transient temperature prescribed on the top surface of the plate, the centroidal deflection for a clamped plate is nearly one-third of that for a simply supported plate, and the maximum magnitude of the axial stress induced at the centroid of the top surface is nearly 40% larger than that for a simply supported plate. For the same time rate of change of the thermal load, steady values of the centroidal deflection and the axial stress are reached much later when heat flux is prescribed than when temperature is prescribed.

REFERENCES

1. H. W. Lavendel and G. C. Goetzel, in, R. F. Hehemann and G. M. Ault (eds.), *High Temperature Materials*, p. 140, Wiley, New York, 1959.
2. Y. Nagase, Y. Ichikawa, A. Kirigai, S. Amada, T. Munekata, and Y. Ahifei, The Mechanical Structures of Bamboo in Viewpoint of Functionally Gradient and Composite Materials, *J. Compos. Mater*., vol. 30, pp. 800–819, 1996.
3. K. Okano and Y. Takagi, Application of SiC-Si Functionally Gradient Material to Thermoelectric Energy Conversion Device, *Electr. Eng. Jpn*, vol. 117, pp. 9–17, 1996.
4. Y. Uchimoto, M. Inaba, A. Tasaka, A. Komura, and Z. Ogumi, Preparation of Functionally Gradient Fluorocarbon Polymer Films by Plasma Polymerization of NF3 and Propylene, *J. Polym. Sci. A*, vol. 34, pp. 193–198, 1996.
5. Y. Toshio, M. Atsuro, H. Matsuno, M. Uo, R. Miyako, Y. Tamura, F. Watari, M. Omori, and T. Kawasaki, Fabrication and Properties of FGM for Biomedical Application, *J. Jpn Soc. Powder Metall*., vol. 47, pp. 1226–1233, 2000.
6. T. Mori and K. Tanaka, Average Stress in Matrix and Average Elastic Energy of Materials with Misfitting Inclusions, *Acta Metall*., vol. 21, pp. 571–574, 1973.
7. R. Hill, A Self-Consistent Mechanics of Composite Materials, *J. Mech. Phys. Solid*, vol. 13, pp. 213–222, 1965.
8. B. Jiang and R. C. Batra, Effective Properties of a Piezocomposite Containing Shape Memory Alloy and Inert Inclusions, *Contin. Mech. Thermodyn*., vol. 14, pp. 87–111, 2002.
9. H. Fröhlich and R. Sack, Theory of the Rheological Properties of Dispersions, *Proc. Roy. Soc. Lond. A*, vol. 185, pp. 415–430, 1946.
10. R. M. Christensen, *Mechanics of Composite Materials*, John Wiley & Sons, New York, 1979.
11. S. S. Vel and R. C. Batra, Exact Solutions for Thermoelastic Deformations of Functionally Graded Thick Rectangular Plates, *AIAA J*., vol. 40, pp. 1421–1433, 2002.
12. S. S. Vel and R. C. Batra, Three-Dimensional Analysis of Transient Thermal Stresses in Functionally Graded Plates, *Int. J. Solid Struct*., vol 40, pp. 7181–7196, 2003.
13. S. S. Vel and R. C. Batra, Three-Dimensional Exact Solution for the Vibration of Functionally Graded Rectangular Plates, *J. Sound Vib*., vol. 272, pp. 703–730, 2004.
14. R. C. Batra, Finite Plane Strain Deformations of Rubberlike Materials, *Int. J. Num. Method Eng*., vol. 15, pp. 145–160, 1980.
15. Y. Ootao, T. Akai, and Y. Tanigawa, Three-Dimensional Transient Thermal Stress Analysis of Nonhomogeneous Hollow Circular Cylinder, *Trans. Jpn Soc. Mech. Eng. A*, vol. 59, pp. 1684–1690, 1993 (in Japanese).
16. Y. Ootao and Y. Tanigawa, Three-Dimensional Transient Thermal Stress Analysis of a Non-homogeneous Hollow Sphere with Respect to a Rotating Heat Source, *Trans. Jpn Soc. Mech. Eng. A*, vol. 460, pp. 2273–2279, 1994 (in Japanese).
17. K.-S. Kim and N. Noda, Green's Function Approach to Three-Dimensional Heat Conduction Equations of Functionally Graded Materials, *J. Thermal Stresses*, vol. 24, pp. 457–477, 2001.
18. Y. Tanigawa, Y. Ootao, and R. Kawamura, Thermal Bending of Laminated Composite Rectangular Plates and Nonhomogeneous Plates Due to Partial Heating, *J. Thermal Stresses*, vol. 14, pp. 285–308, 1991.
19. T. G. Rogers, P. Watson, and A. J. M. Spencer, Exact Three-Dimensional Elasticity Solutions for Bending of Moderately Thick Inhomogeneous and Laminated Strips under Normal Pressure, *Int. J. Solid Struct*., vol. 32, pp. 1659–1673, 1995.
20. J. N. Reddy and Z. Q. Cheng, Three-Dimensional Thermomechanical Deformations of Functionally Graded Rectagnular Plates, *Eur. J. Mech. A*, vol. 20, pp. 841–855, 2001.
21. Z. Q. Cheng and R. C. Batra, Deflection Relationships Between the Homogeneous Kirchhoff Plate Theory and Different Functionally Graded Plate Theories, *Arch. Mech*., vol. 52, pp. 143–158, 2000.
22. J. N. Reddy, Analysis of Functionally Graded Plates, *Int. J. Num. Method Eng*., vol. 47, pp. 663–684, 2000.

23. L. F. Qian, R. C. Batra, and L. M. Chen, Static and Dynamic Deformations of Thick Functionally Graded Elastic Plates by Using Higher-Order Shear and Normal Deformable Plate Theory and Meshless Local Petrov-Galerkin Method, *Compos. B*, vol. 35, 2005 (to appear).
24. R. C. Batra and S. Vidoli, Higher Order Piezoelectric Plate Theory Derived from a Three-Dimensional Variationl Principle, *AIAA J.*, vol. 40, pp. 91–104, 2002.
25. C. T. Loy, K. Y. Lam, and J. N. Reddy, Vibration of Functionally Graded Cylindrical Shells, *Int. J. Mech. Sci.*, vol. 41, pp. 309–324, 1999.
26. S. N. Atluri and S. P. Shen, *The Meshless Local Petrov-Galerkin (MLPG) Method*, Tech Science Press, Encino, CA, 2002.
27. G. R. Liu, *Mesh Free Methods*, CRC Press, Boca Raton, FL, 2003.
28. T. Belytschko, Y. Y. Lu, and L. Gu, Element-Free Galerkin Methods, *Int. J. Num. Method Eng.*, vol 37, pp. 229–256, 1994.
29. C. A. Durate and J. T. Oden, H-p Clouds—An *hp* Meshless Method, *Num. Method Part. Diff. Eq.*, vol. 12, pp. 673–705, 1996.
30. W. K. Liu, S. Jun, and Y. F. Zhang, Reproducing Kernel Particle Methods, *Int. J. Num. Method Eng.*, vol. 20, pp. 1081–1106, 1995.
31. L. Lucy, A Numerical Approach to Testing the Fission Hypothesis, *Astronom. J.*, vol. 82, pp. 1013–1024, 1977.
32. R. A. Gingold and I. J. Monagham, Smooth Particle Hydrodynamics: Theory and Applications to Non-spherical Stars, *Mon. Not. R. Astron. Soc.*, vol. 181, pp. 375–389, 1977.
33. B. Nayroles, G. Touzot, and P. Villon, Generalizing the Finite Element Method: Diffuse Approximation and Diffuse Elements, *Comput. Mech.*, vol. 10, pp. 307–318, 1992.
34. J. M. Melenk and I. Babuska, The Partition of Unity Finite Element Method: Basic Theory and Applications, *Comput. Method Appl. Mech. Eng.*, vol. 139, pp. 289–314, 1996.
35. N. Sukumar, B. Moran, and T. Belytschko, The Natural Element Method in Solid Mechanics, *Int. J. Num. Method Eng.*, vol. 43, pp. 839–887, 1998.
36. H. Wendland, Piecewise Polynomial, Positive Definite and Compactly Supported Radial Basis Functions of Minimal Degree, *Adv. Comput. Method*, vol. 4, pp. 389–396, 1995.
37. S. N. Atluri and T. Zhu, A New Meshless Local Petrov-Galerkin (MLPG) Approach in Computational Mechanics, *Comput. Mech.*, vol. 22, pp. 117–127, 1998.
38. L. F. Qian and R. C. Batra, Three-Dimensional Transient Heat Conduction in a Functionally Graded Thick Plate with a Higher-Order Plate Theory and a Meshless Local Petrov-Galerkin Method, submitted for publication.
39. R. D. Mindlin and M. A. Medick, Extensional Vibrations of Elastic Plates, *J. Appl. Mech.*, vol. 26, pp. 145–151, 1959.
40. R. C. Batra, S. Vidoli, and F. Vestroni, Plane Waves and Modal Analysis in Higher-Order Shear and Normal Deformable Plate Theories, *J. Sound Vib.*, vol. 257, pp. 63–88, 2002.
41. J. S. Yang and R. C. Batra, Mixed Variational Principles in Nonlinear Piezoelectricity, *Int. J. Nonlinear Mech.*, vol. 30, pp. 719–726, 1995.
42. P. Lancaster and K. Salkauskas, Surfaces Generated by Moving Least Squares Method, *Comput. Mech.*, vol. 37, pp. 141–158, 1981.
43. R. C. Batra and H.-K. Ching, Analysis of Elastodynamic Deformations near a Crack-Notch Tip by the Meshless Local Petrov-Galerkin (MLPG) Method, *Comput. Model. Eng. Sci.*, vol. 3, pp. 717–730, 2002.
44. H. Hatta and M. Taya, Effective Thermal Conductivity of a Misoriented Short Fiber Composite, *J. Appl. Phys.*, vol. 58, pp. 2478–2486, 1985.
45. B. W. Rosen and Z. Hashin, Effective Thermal Expansion Coefficients and Specific Heats of Composite Materials, *Int. J. Eng. Sci.*, vol. 8, pp. 157–173, 1970.
46. R. C. Batra and T. S. Geng, Enhancement of the Dynamic Buckling Load for a Plate by Using Piezoceramic Actuators, *Smart Mater. Struct.*, vol. 10, pp. 925–933, 2001.
47. R. C. Batra and T. S. Geng, Comparison of Active Constrained Layer Damping by Using Extension and Shear Mode Actuators, *J. Intell. Mater. Struct.*, vol. 13, pp. 349–367, 2002.

48. L. F. Qian, R. C. Batra, and L. M. Chen, Elastostatic Deformations of a Thick Plate by Using a Higher-Order Shear and Normal Deformable Plate Theory and Two Meshless Local Petrov-Galerkin (MLPG) Methods, *Comput. Model. Eng. Sci.*, vol. 4, pp. 161–176, 2003.
49. L. F. Qian, R. C. Batra, and L. M. Chen, Free and Forced Vibrations of Thick Rectangular Plates by Using Higher-Order Shear and Normal Deformable Plate Theory and Meshless Local Petrov-Galerkin (MLPG) Method, *Comput. Model. Eng. Sci.*, vol. 4, pp. 519–534, 2003.
50. L. F. Qian, R. C. Batra, and L. M. Chen, Analysis of Cylindrical Bending Thermoelastic Deformations of Functionally Graded Plates by a Meshless Local Petrov-Galerkin Method, *Computational Mechanics*, 33, 263–273, 2004.
51. L. F. Qian and R. C. Batra, Design of Bidirectional Functionally Graded Plate for Optimal Natural Frequencies, *J. of Sound and Vibration* (in press).
52. R. C. Batra and B. M. Love, Adiabatic Shear Bands in Functionally Graded Materials, *J. of Thermal Stresses* (in press).
53. R. C. Batra, M. Porfiri, and D. Spinello, Treatment of Material Discontinuity in Two Meshless Local Petrov-Galerkin (MLPG) Formulations of Axisymmetric Transient Heat Conduction, *Int. J. for Numerical Methods in Engineering* (in press).
54. Y. Krongauz and T. Belyschko, EFG approximation with discontinuous derivatives, *Int. J. for Numerical Methods in Engineering*, vol. 41, pp. 1215–1233, 1998.
55. R. C. Batra and J. Jin, Natural Frequencies of a Functionally Graded Rectangular Plate, *J. of Sound and Vibration* (in press).
56. G. M. Zhang and R. C. Batra, Modified Smoothed Particle Hydrodynamics Method and Its Application to Transient Problems, *Computational Mechanics* (in press).
57. R. C. Batra and G. M. Zhang, Analysis of Adiabatic Shear Bands in Elastothermoviscoplastic Materials by Modified Smoothed Particle Hydrodynamics Method, *J. of Computational Physics*, (in press).

APPENDIX

Expressions for the orthonormalized Legendre polynomials $L_0(z),\ L_1(z), \ldots, L_5(z)$ are

$$L_0(z) = \frac{1}{\sqrt{h}}$$

$$L_1(z) = \sqrt{\frac{3}{h}}\frac{2z}{h}$$

$$L_2(z) = \sqrt{\frac{5}{h}}\left(12\frac{z^2}{h^2} - 1\right)$$

$$L_3(z) = \sqrt{\frac{7}{h}}\left(-\frac{3z}{h} + 20\frac{z^3}{h^3}\right)$$

$$L_4(z) = \sqrt{\frac{3}{h}}\left(\frac{3}{8} - \frac{15z^2}{h^2} + 70\frac{z^4}{h^4}\right)$$

$$L_5(z) = \sqrt{\frac{11}{h}}\left(\frac{15z}{4h} - 70\frac{z^3}{h^3} + 252\frac{z^5}{h^5}\right)$$